

SCoBi-Veg: A Generalized Bistatic Scattering Model of Reflectometry From Vegetation for Signals of Opportunity Applications

Mehmet Kurum¹, *Senior Member, IEEE*, Manohar Deshpande, *Senior Member, IEEE*, Alicia T. Joseph, Peggy E. O'Neill, *Fellow, IEEE*, Roger H. Lang, *Life Fellow, IEEE*, and Orhan Eroglu, *Member, IEEE*

Abstract—SCoBi-Veg stands for Signals of opportunity Coherent Bistatic scattering model for Vegetated terrains. It simulates polarimetric reflectometry of vegetation canopy over a flat ground using a Monte Carlo scheme. The model is aimed at assessing the value of navigation and communication satellite Signals of Opportunity in a range of frequencies from P- to S-bands for remote sensing of a number of geophysical land parameters such as soil moisture and biomass. A fully polarimetric expression for bistatic scattering from a vegetation canopy is first formulated for a general case and is then specialized to the practical case of ground-based/low-altitude platforms with passive receivers overlooking vegetation using the signals transmitted from large distances. Using analytical wave theory in conjunction with distorted Born approximation, the transmit and receive antenna effects (i.e., polarization crosstalk/mismatch, orientation, and altitude) are explicitly accounted for. The forward model developed here enables the understanding of the effect of different geophysical parameters and system configurations on the coherent and incoherent components of the reflected signatures. It can thus help developing robust inverse algorithm for extraction of soil moisture and biomass. The model is applied to P-band signals of geostationary communication satellites to describe polarimetric reflections from tree canopies as observed from down-looking platforms at various altitudes. The relative contributions of diffuse and specular scattering on total reflected power and reflectivity are quantified for various observing scenarios.

Index Terms—Bistatic, diffuse, polarimetric, Signals of Opportunity (SoOp), specular, vegetation.

Manuscript received December 25, 2017; revised March 31, 2018 and July 4, 2018; accepted August 5, 2018. The research described and the resulting data presented herein, unless otherwise noted, was funded under PE 0602784A, Project T53 “Military Engineering Applied Research”, Task 08 under Contract W56HZV-17-C-0095, by the US Army Engineer Research and Development Center (ERDC) and the US ARMY Tank Automotive Research Development & Engineering Center (TARDEC). The work described in this document/presentation was conducted at Mississippi State University. Permission was granted by ERDC and TARDEC to publish this information. Approved for public release; distribution unlimited. (*Corresponding author: Mehmet Kurum.*)

M. Kurum and O. Eroglu are with the Department of Electrical and Computer Engineering, Mississippi State University, Mississippi State, MS 39762 USA (e-mail: kurum@ece.msstate.edu).

M. Deshpande is with the Microwave Instrument Technology Branch (Code 555), NASA Goddard Space Flight Center, Greenbelt, MD 20771 USA.

A. T. Joseph and P. E. O'Neill are with the Hydrological Sciences Laboratory (Code 617), NASA Goddard Space Flight Center, Greenbelt, MD 20771 USA.

R. H. Lang is with the Department of Electrical and Computer Engineering, George Washington University, Washington, DC 20052 USA.

Color versions of one or more of the figures in this paper are available online at <http://ieeexplore.ieee.org>.

Digital Object Identifier 10.1109/TGRS.2018.2864631

I. INTRODUCTION

SIGNALS of Opportunity (SoOp)-based systems have emerged in recent years as a new domain of microwave remote sensing with great potential to realize the earth science community’s need for global geophysical parameter retrieval at high spatiotemporal scales [1], [2]. The key principle of the SoOp approach is to receive and further extract information from free illuminators whose signal reflects off the earth surface. Unlike traditional microwave remote sensing, the existing signal sources are exploited in bistatic configuration in which the transmitter and the receiver are separated by significant distance. SoOp systems are a powerful, cost-effective approach because they only require the development of a passive receiver, analysis algorithm, and no on-board transmitter. SoOp concept has been widely used for collecting or modeling of Global Navigation Satellite System (GNSS) signal reflections over the ocean surface for estimating wind vectors or altimetry since the 1990s. It has been implemented in technology demonstration experiments, TechDemoSat-1 (TDS-1) [3] and United Kingdom Disaster Monitoring Constellation [4], and a dedicated ocean mission [Cyclone GNSS (CYGNSS)] [5] from space.

The application of GNSS reflectometry (GNSS-R) to other geophysical variables such as soil moisture, vegetation, wetland extent, and snow has also been studied from ground and airborne systems under several different measurement configurations [6]. For instance, interference patterns between direct and reflected signals are exploited using either geodetic or specifically designed GNSS receivers located on a tower to derive soil moisture over bare and vegetated surfaces [7]–[11]. In addition, airborne and balloon experiments have been used to evaluate the potential of GNSS-R methodologies for larger scale applications [12], [13]. Most recently, the qualitative analysis of TDS-1 data over land, in conjunction with other satellite products such as soil moisture data from Soil Moisture Ocean Salinity level 3 and normalized difference vegetation index data from Moderate Resolution Imaging Spectroradiometer or Landsat, has demonstrated that the reflected signal has an extremely large dynamic range over land [14]–[16]. In addition, the large amount of land observations by the recent CYGNSS mission provides investigators’ opportunities to further infer the sensitivity of GNSS-R measurements to various land features from space.

There is increasing interest to extend these techniques originally developed for L-band GNSS signals to digital transmissions from communication satellites in other bands [17]. For instance, SoOp methods have been applied to communication satellite broadcasts in S- and Ku-bands and used to demonstrate remote sensing of ocean winds, significant wave height, and sea surface height [18], [19]. The P-band signals transmitted by the Military Satellite Communication series of satellites have been proposed to measure root-zone soil moisture through heavy vegetation by recording reflected signals using a simple passive microwave receiver [20]–[22]. Furthermore, P-band signals have been used to demonstrate remote sensing of snow water equivalent by analysis of the phase change of the reflected signal [23].

There are a host of navigation and communications satellites illuminating multiple regions of the globe all the time. Furthermore, these satellites span a wide range of the microwave spectrum. Hence, each one of these satellites is a potential candidate for doing different earth science remote sensing. In order to fully leverage the potential of these SoOp transmitters, it is advantageous to develop bistatic scattering models of earth terrain that describe land interactions with the signals at different frequencies in the specular direction. In other words, using scattering models, we can: 1) explore new measurement techniques and configurations; 2) understand the advantages and limitations of each technique; 3) identify the optimum frequencies and signal properties that could help determine the parameters of interest; and 4) deliver sets of test data for training retrieval algorithms. With these goals in mind, we recently developed a coherent bistatic vegetation scattering model, based on a Monte Carlo simulation, to compute polarimetric bistatic reflectometry [24]. Indeed, due to the scarcity of available bistatic data, it appears that scattering models are a critical step in the advancement of these studies and in the design of future missions or field campaigns.

Despite the somewhat large amount of existing data for soil moisture or vegetation biomass retrieval from monostatic active/passive microwave systems and numerous theoretical models (dating back to the 1970s), bistatic scattering models capable of estimating land parameters from space are still in relatively early stages of development. Very few models which can handle bistatic configurations have so far been developed and can be grouped into two basic categories. The first group [25]–[29] is incoherent models that are based on radiative transfer (RT) theory. This approach is a heuristic method based on the law of energy conservation, so it supplies no phase information, but the vector form of RT models is capable of simulating polarimetric data. The second group [24], [30] is coherent models that are based on analytical wave theory in conjunction with the distorted Born approximation and perform coherent sum of the scattered fields. They provide complex field quantities and thus include both amplitude and phase information. This enables one not only to simulate polarimetric bistatic reflectometry for various polarization combinations but also to realize interferometric or beamforming techniques.

In [25], Michigan Microwave Canopy Scattering (MIMICS) model, which is based on the first-order RT theory, is extended to bistatic geometry (hence called bi-MIMICS). The model has been applied to tree canopies at L-, C-, and X-bands with linear polarizations. The bistatic scattering results are compared with those in the backscatter direction to find out optimum sensing configuration for forest biomass estimation. Wu and Jin [29] modified bi-MIMIC model by including combination of circular and linear polarizations of transmitter/receiver to investigate the effect of various observation angles and polarization combinations on the bistatic reflectometry over Aspen stands.

In [26], an RT-based multiple-scattering model (called Tor Vergeta), which is intrinsically bistatic, is extended to consider specular scattering by including circular polarization in specular direction, focusing on GNSS-R applications to biomass monitoring of forests. The model combines the scattering and extinction properties of each scatterer using the matrix doubling algorithm. Guerriero *et al.* [27] employed the Tor Vergeta model to perform simulations of the scattering coefficient of corn at linear polarizations, over a wide range of observation angles at L- and C-bands. Later, Pierdicca *et al.* [28] developed a simulator (called SAVERS) for GNSS reflections from bare and vegetated soils, which uses the Tor Vergeta model with circular polarization. The polarization synthesis technique, applied to take antenna polarization mismatch and crosstalk into account, has been presented. Preliminary assessment of the simulator is successfully demonstrated against the field data acquired over sunflower plants during a growing cycle.

Thirion-Lefevre *et al.* [30] studied bistatic scattering by forested areas using a coherent scattering model called COBISMO, which is an extension of previous developed coherent backscatter model. They considered linear polarization and analyzed radiometric and polarimetric aspects of bistatic scattering coefficients of forest canopies at P-band to check the physical relevance of the model behavior. The present model, Signals of opportunity Coherent Bistatic scattering model for Vegetated terrains (SCoBi-Veg), falls in the same category with COBISMO, but includes more comprehensive antenna characteristics as well as circular polarization since the SoOp transmitters are often circularly polarized and the receiver antennas cannot be constructed to produce pure polarization states.

The SCoBi-Veg model calculates the received complex field in three main contributions: 1) direct term; 2) specular term; and 3) diffuse term by explicitly accounting for both antenna and scene characteristics. The first contribution represents the line of sight or the shortest path between the antennas while the second term denotes the scattering along the specular direction. Finally, the diffusely scattered waves arrive at the receiver antenna from a wide range of angles in both azimuth and elevation due to scattering from the illuminated volume. An average diffuse term is obtained by a sufficient number of realizations of vegetation through Monte Carlo simulations. In received reflected field, the antenna characteristics and orientation play a key role. For instance, for ground-based systems, the antenna radiation pattern projected on the surface is not uniformly distributed in phase, amplitude, or polarization.

The bistatic radar coefficient calculated by the model thus needs to have the antenna characteristics embedded in it as well as the statistical and physical properties of the terrain to mimic the real measurement setting. Previous studies have usually assumed plane wave illumination/scattering, and/or ignored such antenna effects. The SCoBi-Veg model considers variations of both the strength and polarization states of the received wave along the beam direction so that the same model could be uniformly applied across different platforms at various altitudes. This is an important step since the ground-based receivers are often used for validation of algorithms to be used by spaceborne observations.

This paper aims at presenting an overview of the newly formulated coherent bistatic vegetation scattering model, i.e., SCoBi-Veg, as well as P-band analysis of polarimetric specular and diffuse contributions for a tree canopy. A companion paper is currently in preparation to provide details of open-source implementation of the SCoBi-Veg model in MATLAB/Octave environment. Section II starts providing explicit expressions of direct, specular, and diffuse contributions to the received field in a general bistatic configuration. The field quantities are then converted to the polarimetric received power in modified Stokes vectors. Section II concludes by specializing the model for geometries where the relative distance of the transmitter to the receiver with respect to the specular ground point is large. This represents the most common observation configuration for SoOp concepts. Section III first introduces the simulation setting and parameters at P-band, and then provides simulation results and discussion of the results. Finally, Section IV summarizes the important aspects of the model and draws conclusions based on the simulated results. Four appendixes are provided at the end to supplement understanding of the model formulation, definitions, and notations.

II. MODEL

In this section, the details of the formulation behind the SCoBi-Veg model will be presented. A general bistatic scattering case is first considered, where two antennas do not have their main beam axis pointing at each other and both of which are overlooking the vegetation. One antenna system is associated with the SoOp transmitter while the other refers to the passive receiver. The vegetation is represented as ensemble of canonical scatterers located above a flat ground. The model calculates direct, specular, and diffuse components of the received complex field for a wide-beam antenna system with nonzero cross-polarization. The model is specialized to the most common SoOp application, where the transmitter is located far away. The local incident angles are assumed to be constant (parallel incident rays) and spreading loss effects due to the incoming wave are ignored, but the spreading loss and sphericity of the scattered wave are considered due to proximity of the receiver platforms that may operate close to the ground. This configuration will represent “plane wave incidence” and “spherical wave scattering.” Furthermore, the formulation considers variations of both the strength and polarization states of the received wave along the beam direction by taking into account for the polarization mismatch

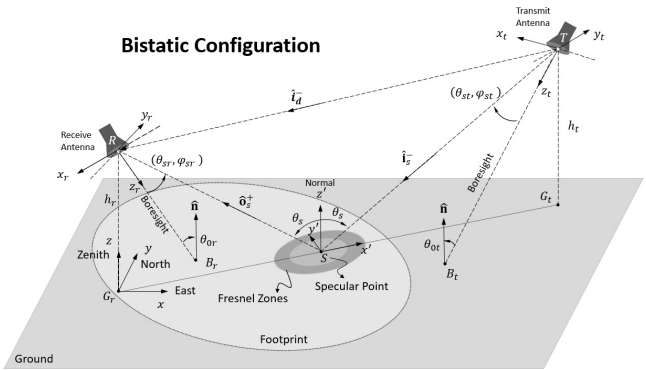


Fig. 1. Arbitrary bistatic antenna configuration.

and crosstalk. Since the model preserves the phase of the scattered field from the canopy, it allows us to calculate various combination of transmit–receive polarization combinations to investigate various polarization signatures.

A. General Case

In this section, we will consider a general bistatic scattering case where two antennas do not have their main beam axis pointing at each other. A step-by-step process will be outlined to obtain the received field when two nonideal antennas are mismatched in polarization. A transmit antenna located at point T (at a height of h_t) is considered to be illuminating the earth surface and another antenna as a receiver located at point R (at a height of h_r) is collecting the scattered field from the surface as depicted in Fig. 1. In this paper, the earth surface is assumed to be planar, mostly valid for ground-based or low-altitude aircraft platforms, while the same formulation can be extended for spaceborne geometries, where the earth curvature is important. In the reference coordinate system (x, y, z) , the zenith (or surface normal $\hat{\mathbf{n}}$) is in $\hat{\mathbf{z}}$ direction while the unit vectors $\hat{\mathbf{x}}$ and $\hat{\mathbf{y}}$ form the ground (xy plane) and are aligned with the local East and North directions, respectively. The reference frame defined here is similar to the standard local east, north, up (ENU) system. The transmit antenna in a coordinate system (x_t, y_t, z_t) points to the ground (point B_t) with the incidence angle $\theta_{0t} = \cos^{-1}(-\hat{\mathbf{n}} \cdot \hat{\mathbf{z}}_t)$ while the receive antenna in a coordinate system (x_r, y_r, z_r) points to the ground (point B_r) with the incidence angle $\theta_{0r} = \cos^{-1}(-\hat{\mathbf{n}} \cdot \hat{\mathbf{z}}_r)$. The main beam (boresight) axis of both antennas is aligned with their own local z coordinates. For notational clarity, unit vectors are bolded with a hat over them while vectors with magnitudes other than one will be bolded only. In addition, the subscript r refers to a quantity associated with the receive antenna, and t is associated with the transmit antenna.

The electric field radiated by an antenna is commonly defined by a spherical coordinate system. The incident wave, having θ_t and φ_t components in transmit antenna frame, travels in the radial direction $\hat{\mathbf{k}}_i$ from the transmitter, while the scattered wave, having θ_r and φ_r components in receive antenna frame, travels in the radial direction $\hat{\mathbf{k}}_o$ toward the receiver. One can write

$$\hat{\mathbf{k}}_i = \hat{\mathbf{x}}_t \sin \theta_t \cos \varphi_t + \hat{\mathbf{y}}_t \sin \theta_t \sin \varphi_t + \hat{\mathbf{z}}_t \cos \theta_t \quad (1.a)$$

$$-\hat{\mathbf{k}}_o = \hat{\mathbf{x}}_r \sin \theta_r \cos \varphi_r + \hat{\mathbf{y}}_r \sin \theta_r \sin \varphi_r + \hat{\mathbf{z}}_r \cos \theta_r \quad (1.b)$$

where the subscript i refers to a quantity associated with incident (transmitted) wave, and o is associated with the scattered (received) wave. The orthonormal unit vectors $(\hat{x}_i, \hat{y}_i, \hat{z}_i)$ and $(\hat{x}_o, \hat{y}_o, \hat{z}_o)$ are defined along the antenna frame axes.

The point S in Fig. 1 denotes the location of the point of reflection that follows the shortest multipath distance from ground. This is called the ‘‘Specular Point,’’ where the incident and reflected waves make the same angle of θ_s with the surface normal. It is determined from simple image theory by confining the discussion to a plane earth. A local coordinate system (x', y', z') centered at the specular point S is also shown. The x' -axis lies along the ground range between the source and the receiver (between projected points G_i and G_o) while the z' -axis is normal to the surface. The angle between the local x' -axis and the reference (ENU) x -axis, $\varphi = \cos^{-1}(\hat{x} \cdot \hat{x}')$, defines the azimuth direction of the transmit antenna from the local East. The orthonormal unit vectors $(\hat{x}', \hat{y}', \hat{z}')$ are defined along the local coordinate axes.

In reality, the energy source illuminates a large region of the surface, depending on the extent of the transmit antenna main beam. Radiation traveling from surface points by any other path than the specular point will travel a longer distance. The difference between any other path length and the shortest distance will form a family of ellipses on the ground. The elliptic zones can be defined around the specular point with unique phase differences (multiples of half-wavelengths) called Fresnel zones. The exact dimensions of the Fresnel ellipses are given in [31] for planar earth. Depending on the surface roughness and vegetation, the number of contributing zones may differ. In addition, the signal received by any SoOp instrument will be in general constrained by footprints of both transmitter and receiver range and Doppler discriminations.

In the present investigation, P-band geostationary transmitter and tower-based receiver are considered as an example scenario (without loss of generality), so both platforms are not moving. Thus, there will be no Doppler shift in the received field. Since the model preserves the phase, Doppler effects can be incorporated in the simulations as well for GNSS-R applications. Thus, only footprint of receiver and range discrimination are considered in the simulations. Range discrimination represents the relative delay with respect to the specular reflection point. As a result, Fresnel zones correspond to range delays that the SoOp instrument discriminates around the specular point. Fresnel zone basically refers to iso-range discrimination areas proportional to a fraction of the wavelength, which can also be based on the chip resolution as done in the GNSS-R community.

Let us now situate some vegetation over the ground plane. In Fig. 2, bistatic scattering over a vegetated landscape is illustrated from a perspective (looking along y') that is perpendicular to the plane containing the receiver, transmitter, and specular point. The canopy is represented as an ensemble of canonical scatterers located above the ground plane. This approach is called ‘‘discrete scatterer’’ where the canopy can consist of randomly distributed branches, stems, leaves, needles, and vertically distributed tree trunks or stalks all having prescribed location and orientation statistics. Leaves are modeled as flat thin dielectric discs [32], [33] and branches,

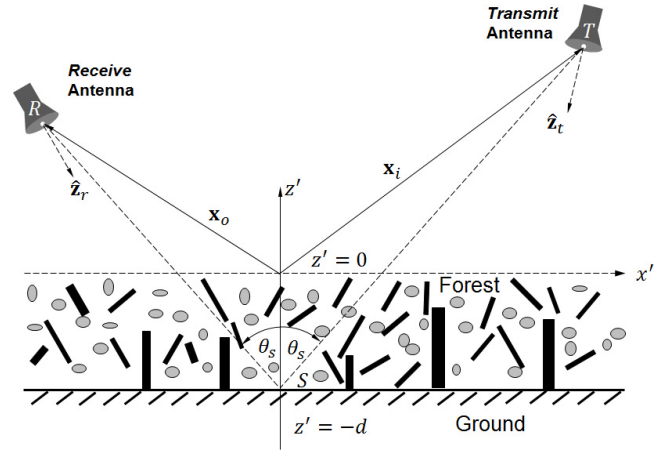


Fig. 2. Representation of a vegetated landscape.

trunks, and stalks are modeled as finitely long lossy-dielectric cylinders [34], [35]. The single-scattering characteristics of these constituents when averaged determine the attenuation and scattering properties of the canopy. The advantage of the discrete approach is that the results are expressed in terms of quantities (plant geometry and orientation statistics) that are related to the biophysical properties of individual plants. These canonical scatterers are assumed to be uniformly distributed throughout the layer.

For sake of convenience, the local coordinate system (x', y', z') is moved to the top surface of the vegetation. The ground ($z = 0$) in ENU is thus denoted by $z' = -d$ plane in local coordinates. The transmit and receive antennas are located at \mathbf{x}_i and \mathbf{x}_o , respectively. The total received field will have direct and multipath components

$$\underline{b} = \begin{bmatrix} b_1 \\ b_2 \end{bmatrix} = \underline{b}_d + \underline{b}_m \quad (2.a)$$

where the direct component is

$$\underline{b}_d = \begin{bmatrix} b_{1d} \\ b_{2d} \end{bmatrix} \quad (2.b)$$

and the multipath component is

$$\underline{b}_m = \begin{bmatrix} b_{1m} \\ b_{2m} \end{bmatrix} \quad (2.c)$$

The elements of \underline{b} vector (i.e., b_1 and b_2) represent network scattering parameters at the physical antenna ports such as port 1 (along x_r -axis) and port 2 (along y_r -axis), respectively, when the antenna is in reception mode. They are complex voltage quantities and their magnitude squares are equal to received power at each port [36]. Throughout the text, the lowercase letters with a single underline denote two-by-one vectors while two-by-two matrices are likewise indicated using lowercase letters with a double underline.

There are two different uses of ‘‘Coherent’’ in this paper. First, with the ‘‘coherent model,’’ it is meant that the absolute phase (complex electric field) of the received signal is preserved. This means that the scattering considers relative positions of scatterers as well as phase change due to reflection and scattering since they are added coherently (summing in

complex electric field). Doppler is another source of phase shift, but not considered in the present investigation. Second, with the “coherent term” as described below, the specular reflection contribution is referred, which comes from a single point only from geometric optics point of view. In other words, the coherent term is simply the expected value of the field.

The multipath component will have coherent (specular reflection) and incoherent (off-specular or diffuse scattering) contributions

$$\underline{b}_m = \underline{b}_m^{\text{coh}} + \underline{b}_m^{\text{inc}} \quad (3.a)$$

where the incoherent contribution is

$$\underline{b}_m^{\text{inc}} = \begin{bmatrix} b_{1m}^{\text{inc}} \\ b_{2m}^{\text{inc}} \end{bmatrix} \quad (3.b)$$

and the coherent contribution is

$$\underline{b}_m^{\text{coh}} = \begin{bmatrix} b_{1m}^{\text{coh}} \\ b_{2m}^{\text{coh}} \end{bmatrix} \quad (3.c)$$

Below, each contribution will be described separately.

1) *Direct Contribution*: This contribution represents the shortest path where the transmitted signal arrives at the receiving antenna directly and is given by

$$\underline{b}_d = K \frac{e^{ik_0 r_d}}{r_d} \underline{g}_r(\hat{\mathbf{k}}_d) \cdot \underline{u}_{t \rightarrow r}(\hat{\mathbf{k}}_d) \cdot \underline{g}_t(\hat{\mathbf{k}}_d) \cdot \underline{e}_t \quad (4.a)$$

where $\hat{\mathbf{k}}_d$ is the unit vector from the transmit antenna to the receiver antenna and the constant K is given by

$$K = i \frac{\lambda_0}{4\pi} \sqrt{G_{0r} \text{EIRP}} \quad (4.b)$$

where $i = \sqrt{-1}$ is the unit complex number, $\text{EIRP} = P_t G_{0t}$ is the equivalent isotropic radiated power (EIRP), λ_0 is the wavelength in free space, P_t is the power transmitted, G_{0t} is the maximum gain of the transmit antenna, G_{0r} is the maximum gain of the receive antenna, r_d is the slant range—the distance between the transmit and receive antennas, and k_0 is the free-space wavenumber i.e., $k_0 = 2\pi/\lambda_0$.

It is important to realize that antennas cannot be constructed to produce pure polarization states [37]. There will always be some nonzero cross-polarization level (crosstalk isolation). Nevertheless, we refer to the antenna, for example, as linearly polarized. Here, it is recognized that we mean “nominally” linear (horizontal) and a cross-polarized (vertical) components will be present. Similarly, for a circularly polarized antenna, we mean “nominally” right-hand circularly polarized (RHCP) and a cross-polarized [left-hand circularly polarized (LHCP)] components will be present. As discussed in Appendix A, the pattern matrices can be constructed to take into account the cross-polarization leakage between ports of the antennas. In (4.a), the receive and transmit antenna patterns are represented by the two-by-two matrices \underline{g}_r and \underline{g}_t , called normalized “voltage” pattern matrices, respectively. Their expressions are given in (A.3) and (A.6) for linearly and circularly polarized antennas, respectively.

The vector $\underline{e}_t = [e_1 \ e_2]^T$ in (4.a), where the superscript T is transpose, defines the nominal polarization state of the transmit antenna ports, and its magnitude is equal to 1.

It represents the polarization state in the main beam direction of the transmit antenna. The polarization, however, varies for increased off-axis angles over the radiation pattern. Due to the orientation of the transmit and the receive antennas, the antenna polarization states are different off the boresight and this will introduce polarization mismatch (hence loss). One can relate polarization states of the transmit and receive antennas through a polarization (field) rotation matrix (see Appendix B). For instance, the rotation matrix from circularly polarized transmit antenna basis ($\hat{\mathbf{u}}_{r1}^R, \hat{\mathbf{u}}_{r2}^L$) to linearly polarized receive antenna basis ($\hat{\mathbf{u}}_{r1}^X, \hat{\mathbf{u}}_{r2}^Y$) can be written as

$$\underline{u}_{t \rightarrow r}(\hat{\mathbf{k}}_d) = \begin{bmatrix} \hat{\mathbf{u}}_{r1}^R \cdot \hat{\mathbf{u}}_{r1}^{X*} & \hat{\mathbf{u}}_{r2}^L \cdot \hat{\mathbf{u}}_{r1}^{X*} \\ \hat{\mathbf{u}}_{r1}^R \cdot \hat{\mathbf{u}}_{r2}^{Y*} & \hat{\mathbf{u}}_{r2}^L \cdot \hat{\mathbf{u}}_{r2}^{Y*} \end{bmatrix} \quad (4.c)$$

where the symbol $*$ represents complex conjugate, the superscripts R , L , X , and Y denote RHCP, LHCP, linear polarization in X -direction (along x -axis port), and linear polarization in Y -direction (along y -axis port), respectively, as defined in Appendix A. In this paper, the antenna y -axis of both transmit and receive frames is chosen to always be parallel to the ground, so that it represents the horizontal polarized port while the other port (x -axis) represents vertical polarization when the antenna is linearly polarized. This scheme is accomplished through antenna rotation matrices as described in Appendix C.

2) *Specular Reflection (Coherent) Contribution*: The coherent contribution represents the reflection from the specular point S on the ground. According to image theory under the assumption that the surface is of infinite extent, it can be written as

$$\underline{b}_m^{\text{coh}} = K \frac{e^{ik_0(r_{st}+r_{sr})}}{(r_{st}+r_{sr})} \underline{g}_r(\hat{\mathbf{o}}_s^+) \cdot \underline{u}_{s \rightarrow r}(\hat{\mathbf{o}}_s^+) \cdot \underline{r}_s(\hat{\mathbf{o}}_s^+, \hat{\mathbf{i}}_s^-) \cdot \underline{u}_{t \rightarrow s}(\hat{\mathbf{i}}_s^-) \cdot \underline{g}_t(\hat{\mathbf{i}}_s^-) \cdot \underline{e}_t \quad (5)$$

where the constant K is defined above in (4.b), and the distances r_{st} and r_{sr} are the ranges from the transmit antenna to the specular point and from the receive antenna to the specular point, respectively.

The wave attenuates as it propagates down from the top of the vegetation to the ground. It then reflects from the surface specularly, and it again attenuates from the ground to the top of the vegetation. The coherent term is essentially attenuated twice by the vegetation. The attenuation and phase change of the coherent wave, propagating in the equivalent medium, is found by calculating the mean field within the medium [38], [39] according to Foldy–Lax approximation [40], [41]. This approach assumes single scattering and azimuthal uniformity, but inhomogeneous along vertical axes. The vegetation canopy can be divided into stratified layers to account for variability along vertical axes. The paulownia trees used in this paper are divided into four layers (one trunk and three canopy layers) as described in Section III.

The propagation and reflection process within the vegetation can be written as a specular reflection matrix

$$\underline{r}_s(\hat{\mathbf{o}}_s^+, \hat{\mathbf{i}}_s^-) = \underline{t}(\hat{\mathbf{o}}_s^+) \cdot \underline{r}_g(\theta_s) \cdot \underline{t}(\hat{\mathbf{i}}_s^-) \quad (6)$$

where \underline{t} is the vegetation transmission matrix and \underline{r}_g is the ground reflection matrix. The unit vectors $\hat{\mathbf{i}}_s^-$ and $\hat{\mathbf{o}}_s^+$

describe the wave propagation in the incoming and outgoing directions, respectively. The superscripts + and − are used to denote the wave modes propagating in the positive and negative z -directions. The subscript s indicates that quantities are calculated for the specular point. The angle θ_s is the angle of reflection at the specular point and can be calculated as

$$\theta_s = \cos^{-1} \{ -\hat{\mathbf{n}} \cdot \hat{\mathbf{i}}_s^- \} = \cos^{-1} \{ \hat{\mathbf{n}} \cdot \hat{\mathbf{o}}_s^+ \} \quad (7)$$

The transmission matrix is responsible for the incident and scattered waves to experience attenuation when they travel in the mean medium [39]. Under the assumption that the scatterers are uniformly distributed in azimuth, the following expression for the one-way transmission matrix is obtained:

$$\underline{\underline{\mathbf{T}}}(\hat{\mathbf{i}}) = \begin{bmatrix} e^{i\Delta\kappa_{zp}(\hat{\mathbf{i}})d} & 0 \\ 0 & e^{i\Delta\kappa_{zq}(\hat{\mathbf{i}})d} \end{bmatrix} \quad (8.a)$$

where d is the depth of the vegetation, $\hat{\mathbf{i}}$ is a unit vector in the direction of propagation (i.e., $\hat{\mathbf{i}}_s^-$ or $\hat{\mathbf{o}}_s^+$), and the exponents of matrix elements are of the form (Foldy–Lax approximation) [40], [41]

$$\Delta\kappa_{zq}(\hat{\mathbf{i}}) = \frac{2\pi}{k_0 \cos \theta} \sum_{\alpha} \rho_{\alpha} \overline{f_{pq}^{\alpha}}(\hat{\mathbf{i}}, \hat{\mathbf{i}}; \beta_{\alpha}) \quad (8.b)$$

where the angle θ is the angle between the unit vector $\hat{\mathbf{i}}$ and z -axis. The summation index α denotes the scatterer types such as leaves, needles, branches, stalks, or trunks. The number density of the scatterer type α is given by ρ_{α} . Here, the quantity $f_{pq}^{\alpha}(\hat{\mathbf{o}}; \hat{\mathbf{i}}; \beta_{\alpha})$ denotes the bistatic scattering amplitude of the scatterer type α , where $\hat{\mathbf{i}}$ is in the direction of the incident wave and $\hat{\mathbf{o}}$ is in the direction of the observation point. The subscripts p and q can be horizontal (H) or vertical (V), and as a result, co- and cross-polarized cases are treated simultaneously.

The quantity β_{α} describes the orientation, size, and position statistics of the scatterer type. The bar over the scattering amplitude denotes ensemble average over the angular and size statistics of the particles. In this paper, the leaves (or needles) are represented by an average-size circular disk (or circular finite cylinder); hence, the averaging is done for orientation angles only. The trunks (or stalks) are vertical and have a typical size. No averaging is, therefore, performed on trunks (or stalks). The branches (if different kinds are included) can be divided into several groups, and each group can have an average length and an average diameter. Orientation averaging can then be performed on each branch group. In other words, orientation of leaves and branches is random but dimension is fixed, trunks dimensions and orientation are fixed, and position of each scatterer is random. Notice that in (8.b), $\overline{f_{pq}^{\alpha}}(\hat{\mathbf{i}}, \hat{\mathbf{i}}; \beta_{\alpha})$ is the forward scattering amplitude of the α th group of scatterers.

In (6), the ground reflection matrix is given by

$$\underline{\underline{\mathbf{r}}}_g(\theta_s) = \begin{bmatrix} \Gamma_{gp}(\theta_s) & 0 \\ 0 & \Gamma_{gq}(\theta_s) \end{bmatrix}. \quad (9.a)$$

It is assumed that the rough surface under the vegetation is smooth and follows Kirchhoff's approximation with a Gaussian height distribution [42]; therefore, diffuse scattering from ground is not accounted for and the reflection coefficient

of the rough surface is expressed with the Fresnel coefficients as

$$\Gamma_{gq}(\theta_s) = r_{gq} e^{-2(k_0 s \cos \theta_s)^2} \quad (9.b)$$

where r_{gq} is the q -polarized Fresnel reflection coefficient of the average dielectric surface, s is the surface rms height, and θ_s is the angle of reflection from the surface, defined in (7). The diffuse surface scattering is attenuated by vegetation twice, and it is not expected to be a strong contributor to the total power unless it is very rough surface and topographic relief exists.

The polarization basis of the receive antenna and the specular ground point along scattered wave ($\hat{\mathbf{o}}_s^+$), denoted by the subscript $s \rightarrow r$, are related by a rotation matrix (see Appendix B) that is given by

$$\underline{\underline{\mathbf{u}}}_{s \rightarrow r}(\hat{\mathbf{o}}_s^+) = \begin{bmatrix} \hat{\mathbf{v}}_o^s \cdot \hat{\mathbf{u}}_{r1}^* & \hat{\mathbf{h}}_o^s \cdot \hat{\mathbf{u}}_{r1}^* \\ \hat{\mathbf{v}}_o^s \cdot \hat{\mathbf{u}}_{r2}^* & \hat{\mathbf{h}}_o^s \cdot \hat{\mathbf{u}}_{r2}^* \end{bmatrix} \quad (10.a)$$

where the local horizontal and vertical polarization in the direction from the specular point to the receiver are, respectively, given by

$$\hat{\mathbf{h}}_o^s = \frac{\hat{\mathbf{n}} \times \hat{\mathbf{o}}_s^+}{|\hat{\mathbf{n}} \times \hat{\mathbf{o}}_s^+|} \quad \text{and} \quad \hat{\mathbf{v}}_o^s = \hat{\mathbf{h}}_o^s \times \hat{\mathbf{o}}_s^+ \quad (10.b)$$

where $\hat{\mathbf{n}} = \hat{\mathbf{z}}'$ and the horizontal polarization vector $\hat{\mathbf{h}}_o^s$ is parallel to the local $x'y'$ plane.

The polarization basis of the transmit antenna and the specular point along the incident wave ($\hat{\mathbf{i}}_s^-$), denoted by the subscript $t \rightarrow s$, are related by a rotation matrix (see Appendix B) that is given by

$$\underline{\underline{\mathbf{u}}}_{t \rightarrow s}(\hat{\mathbf{i}}_s^-) = \begin{bmatrix} \hat{\mathbf{u}}_{t1} \cdot \hat{\mathbf{v}}_i^{s*} & \hat{\mathbf{u}}_{t2} \cdot \hat{\mathbf{v}}_i^{s*} \\ \hat{\mathbf{u}}_{t1} \cdot \hat{\mathbf{h}}_i^s & \hat{\mathbf{u}}_{t2} \cdot \hat{\mathbf{h}}_i^s \end{bmatrix} \quad (11.a)$$

where the local horizontal and vertical polarization in the direction from transmitter to the specular point are, respectively, given by

$$\hat{\mathbf{h}}_i^s = \frac{\hat{\mathbf{i}}_s^- \times \hat{\mathbf{n}}}{|\hat{\mathbf{i}}_s^- \times \hat{\mathbf{n}}|} \quad \text{and} \quad \hat{\mathbf{v}}_i^s = \hat{\mathbf{i}}_s^- \times \hat{\mathbf{h}}_i^s \quad (11.b)$$

where the horizontal polarization vector $\hat{\mathbf{h}}_i^s$ is parallel to local $x'y'$ plane.

3) *Diffuse Scattering (Incoherent) Contribution*: The diffusely scattered waves arrive at the receiver antenna from a wide range of angles in both azimuth and elevation due to scattering from the illuminated volume within the contributing Fresnel zones. In “discrete scatterer” modeling [39], [43], the vegetation layer is usually replaced by a slab of equivalent homogenous medium by the Foldy–Lax theory. Using analytical wave theory in conjunction with distorted Born approximation [39], the transmit and receive antenna effects (i.e., polarization, orientation, and shape) can be explicitly accounted for.

Let us consider the geometry of the problem, shown in Fig. 3, where a single scatterer of type α is embedded at point P_{α} in the medium over the half-space. The position vector is given by $\mathbf{r}_{\alpha} = x_{\alpha}\hat{\mathbf{x}}' + y_{\alpha}\hat{\mathbf{y}}' - z_{\alpha}\hat{\mathbf{z}}'$ in local coordinates.

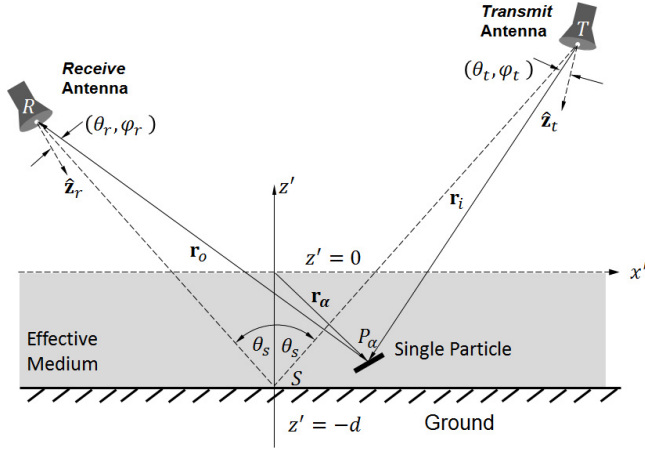


Fig. 3. Scattering from a single particle immersed in the slab of mean medium over a flat ground surface.

An expression for the received field due to this single particle was obtained by employing distorted Born approximation in [44] with the assumption that the regular far-field conditions hold, i.e., each scatterer in the vegetation layer is in the far-zone of the transmit antenna and the receive antenna is also in the far-zone of each scatterer within the layer. The energy source illuminates a large region of surface, inducing currents that radiate in all directions. At any point in space, the reflected field is sum of the radiation from these induced currents according to the Huygens principle. The scattered plane wave of propagation arises as a consequence of all incident plane waves of differing propagation vectors being scattered by the medium into observation direction. If the scatterer is in the far field of the transmit antenna, the double integral involving the transverse wavenumber of the incident wave can be evaluated asymptotically by the method of stationary phase. In addition, with an assumption on the particles such that each particle is uniformly illuminated by the incident wave, the magnitude of the mean wave is essentially constant in the vicinity of the particle. In addition, the antennas with narrow beam and pure polarization state were considered in [44].

The results in [44] are here adapted to a general case where both antennas are considered to be wide-beam with nonzero cross-polarized components. This implies that the strength and polarization of the transmitted and received waves depend on the antenna properties along the beam direction. Summing the result of the single particle scattering over all types and particles and taking into account the polarization mismatch (rotation matrices) and the polarization crosstalk (antenna pattern matrices with co- and cross-polarization components) lead to the following:

$$\begin{aligned} \underline{b}_m^{\text{inc}} = & K \frac{e^{ik_0(r_{st} + r_{sr})}}{r_{st}r_{sr}} \sum_{\alpha} \sum_{n=1}^{N_{\alpha}} \sum_x B_{\alpha,n}^x \\ & \times \left[\underline{g}_r(\hat{\mathbf{o}}_x) \cdot \underline{u}_{p \rightarrow r}(\hat{\mathbf{o}}_x) \cdot \underline{s}_{\alpha,n}^x(\hat{\mathbf{o}}_x, \hat{\mathbf{i}}_x) \cdot \underline{u}_{t \rightarrow p}(\hat{\mathbf{i}}_x) \cdot \underline{g}_t(\hat{\mathbf{i}}_x) \cdot \underline{e}_t \right] \end{aligned} \quad (12)$$

where the constant K and the distances r_{st} and r_{sr} are defined above. The summation indices α , n , and x denote the types of particles, particle number of type α , and the scattering

mechanisms, respectively. N_{α} is the total number of particles of type α within the illuminated volume around the specular point. The normalized “voltage” pattern matrices, \underline{g}_t and \underline{g}_r , of transmit and receive antennas are given in Appendix A and can be linearly or circularly polarized as discussed earlier. The strengths of the incident and scattered waves at each particle are directly proportional to the value of the antenna patterns along that direction.

The wave from each particle follows four distinct paths before arriving at the receiver, denoted by $x \in \{\text{dd}, \text{rd}, \text{dr}, \text{rr}\}$. Each mechanism is described by the following scattering matrices:

$$\underline{s}_{\alpha,n}^{\text{dd}}(\hat{\mathbf{o}}_a^+, \hat{\mathbf{i}}_a^-) = \underline{t}(\hat{\mathbf{o}}_a^+) \cdot \underline{f}_{\alpha}(\hat{\mathbf{o}}_a^+, \hat{\mathbf{i}}_a^-; \beta_{\alpha,n}) \cdot \underline{t}(\hat{\mathbf{i}}_a^-) \quad (13.a)$$

$$\begin{aligned} \underline{s}_{\alpha,n}^{\text{dr}}(\hat{\mathbf{o}}_a^+, \hat{\mathbf{i}}_{aI}^+) = & \underline{t}(\hat{\mathbf{o}}_a^+) \cdot \underline{f}_{\alpha}(\hat{\mathbf{o}}_a^+, \hat{\mathbf{i}}_{aI}^+; \beta_{\alpha,n}) \\ & \cdot \underline{r}_g(\hat{\mathbf{i}}_{aI}^+) \cdot \underline{t}(\hat{\mathbf{i}}_{aI}^+) \end{aligned} \quad (13.b)$$

$$\begin{aligned} \underline{s}_{\alpha,n}^{\text{rd}}(\hat{\mathbf{o}}_{aI}^-, \hat{\mathbf{i}}_a^-) = & \underline{t}(\hat{\mathbf{o}}_{aI}^-) \cdot \underline{r}_g(\hat{\mathbf{o}}_{aI}^-) \\ & \cdot \underline{f}_{\alpha}(\hat{\mathbf{o}}_{aI}^-, \hat{\mathbf{i}}_a^-; \beta_{\alpha,n}) \cdot \underline{t}(\hat{\mathbf{i}}_a^-) \end{aligned} \quad (13.c)$$

$$\begin{aligned} \underline{s}_{\alpha,n}^{\text{rr}}(\hat{\mathbf{o}}_{aI}^-, \hat{\mathbf{i}}_{aI}^+) = & \underline{t}(\hat{\mathbf{o}}_{aI}^-) \cdot \underline{r}_g(\hat{\mathbf{o}}_{aI}^-) \cdot \underline{f}_{\alpha}(\hat{\mathbf{o}}_{aI}^-, \hat{\mathbf{i}}_{aI}^+; \beta_{\alpha,n}) \\ & \cdot \underline{r}_g(\hat{\mathbf{i}}_{aI}^+) \cdot \underline{t}(\hat{\mathbf{i}}_{aI}^+) \end{aligned} \quad (13.d)$$

where the unit vectors are defined as

$$\hat{\mathbf{i}}_a^- = \frac{\mathbf{r}_i}{r_i}, \quad r_i = |\mathbf{r}_i| = |\mathbf{r}_a - \mathbf{x}_i| \quad (14.a)$$

$$\hat{\mathbf{o}}_a^+ = \frac{\mathbf{r}_o}{r_o}, \quad r_o = |\mathbf{r}_o| = |\mathbf{r}_a - \mathbf{x}_o| \quad (14.b)$$

$$\hat{\mathbf{i}}_{aI}^+ = \frac{\mathbf{r}_{iI}}{r_{iI}}, \quad r_{iI} = |\mathbf{r}_{iI}| = |\mathbf{r}_a - \mathbf{x}_{iI}| \quad (14.c)$$

$$\hat{\mathbf{o}}_{aI}^- = \frac{\mathbf{r}_{oI}}{r_{oI}}, \quad r_{oI} = |\mathbf{r}_{oI}| = |\mathbf{r}_a - \mathbf{x}_{oI}| \quad (14.d)$$

and where the superscripts $+$ and $-$ are used to denote the wave modes propagating in the positive and negative z -directions, respectively. The subscript I is introduced in the notation to refer to the auxiliary image antenna.

Fig. 4 illustrates the scattering mechanisms for a single particle. The reflected paths are illustrated by the image antenna representation, where the images of the transmit and receive antennas with respect to ground are positioned at $\mathbf{x}_{iI} = \mathbf{x}_i - 2(\mathbf{x}_i \cdot \hat{\mathbf{z}}' + d)\hat{\mathbf{z}}'$ and $\mathbf{x}_{oI} = \mathbf{x}_o - 2(\mathbf{x}_o \cdot \hat{\mathbf{z}}' + d)\hat{\mathbf{z}}'$, respectively. In order to account for the attenuation of the reflected components, an image medium is included in Fig. 4. Each scattering mechanism can be visualized as follows.

- 1) *Single Bounce Contribution [see (13.a)]*: Direct–direct (dd) term follows the path TP_aR . The field travels in the direction of $\hat{\mathbf{i}}_x = \hat{\mathbf{i}}_a^-$ toward the particle of type α , located at \mathbf{r}_a , and then the incident field is bistatically scattered from this particle and travels in the direction of $\hat{\mathbf{o}}_x = \hat{\mathbf{o}}_a^+$ toward the receive antenna.
- 2) *Double Bounce Contributions [see (13.b) and (13.c)]*: It includes two mechanisms such as reflected-direct (dr) and direct-reflected (rd) terms. The first mechanism follows the path $T_I P_a R$. The field incident on the particle in the direction of $\hat{\mathbf{i}}_x = \hat{\mathbf{i}}_{aI}^+$ from the image of the transmit antenna is reflected from the ground and

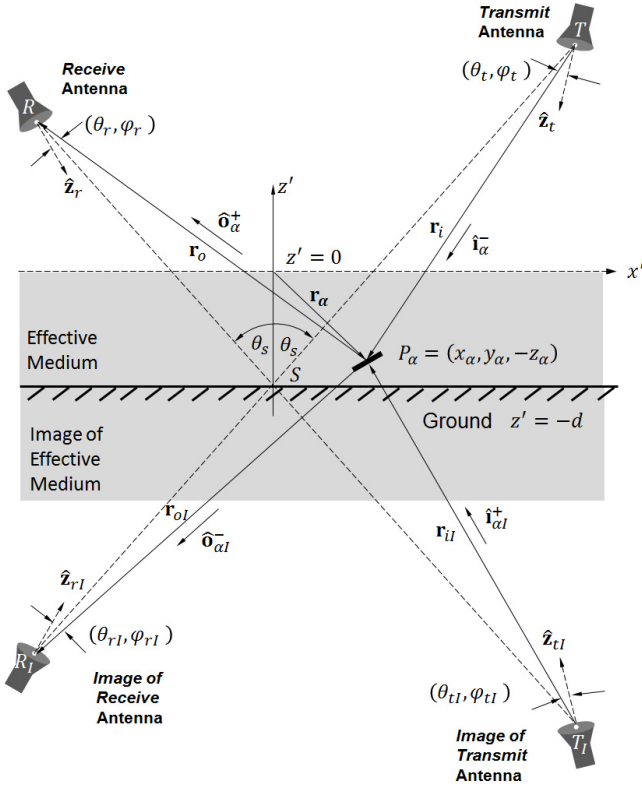


Fig. 4. Scattering mechanisms and vector definitions for bistatic antenna configuration.

bistatically scattered from the particle in the direction of $\hat{\mathbf{o}}_x = \hat{\mathbf{o}}_\alpha^+$ toward the receive antenna. The second mechanism follows the path $TP_\alpha R_I$. The field incident on the particle in the direction of $\hat{\mathbf{i}}_x = \hat{\mathbf{i}}_\alpha^-$ is bistatically scattered from the particle in the direction of $\hat{\mathbf{o}}_x = \hat{\mathbf{o}}_{\alpha I}^-$ toward the image of receive antenna after reflection from the ground.

- 3) *Triple Bounce Contribution* [see (13.d)]: Reflected-reflected (rr) term follows the path $T_I P_\alpha R_I$. The field incident on the particle in the direction of $\hat{\mathbf{i}}_x = \hat{\mathbf{i}}_{\alpha I}^+$ from the image of the transmit antenna is reflected from the ground and bistatically scattered from the particle in the direction of $\hat{\mathbf{o}}_x = \hat{\mathbf{o}}_{\alpha I}^-$ toward the image of receive antenna after reflection from the ground. It involves double reflection from the ground.

The bistatic scattering from the particle of type α is described by a bistatic scattering amplitude matrix $\underline{\underline{f}}_\alpha(\hat{\mathbf{o}}_x, \hat{\mathbf{i}}_x; \beta_{\alpha,n})$ as

$$\underline{\underline{f}}_\alpha(\hat{\mathbf{o}}_x, \hat{\mathbf{i}}_x; \beta_{\alpha,n}) = \begin{bmatrix} f_{VV}^\alpha(\hat{\mathbf{o}}_x, \hat{\mathbf{i}}_x; \beta_{\alpha,n}) & f_{VH}^\alpha(\hat{\mathbf{o}}_x, \hat{\mathbf{i}}_x; \beta_{\alpha,n}) \\ f_{HV}^\alpha(\hat{\mathbf{o}}_x, \hat{\mathbf{i}}_x; \beta_{\alpha,n}) & f_{HH}^\alpha(\hat{\mathbf{o}}_x, \hat{\mathbf{i}}_x; \beta_{\alpha,n}) \end{bmatrix} \quad (15)$$

where the bistatic amplitude $f_{pq}^\alpha(\hat{\mathbf{o}}_x, \hat{\mathbf{i}}_x; \beta_{\alpha,n})$ is defined above. The quantities p and q denote the local polarization states along incident ($\hat{\mathbf{i}}_x$) and scattering ($\hat{\mathbf{o}}_x$) directions, respectively, and can be horizontal (H) or vertical (V). As stated above, the quantity $\beta_{\alpha,n}$ describes the orientation, size, and position

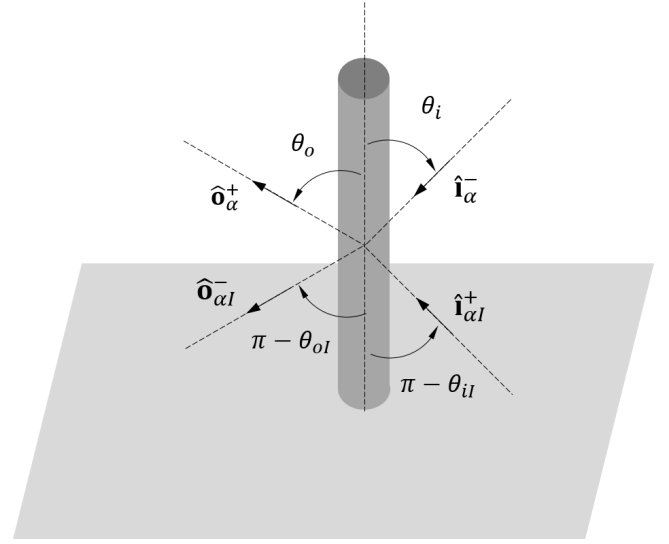


Fig. 5. Unit scattering vector definitions.

statistics of the scatterer type. Note that the polarization of scattering amplitude is given in terms of linear polarization since polarization in the local ground frame is defined with linear polarization basis only.

The ground reflection matrix $\underline{\underline{r}}_g$ is defined in (9) and the transmission matrix $\underline{\underline{t}}$ for the particle located at \mathbf{r}_α (the point P_α) is given by

$$\underline{\underline{t}}(\hat{\mathbf{i}}) = \begin{bmatrix} e^{i\Delta\kappa_{zp}(\hat{\mathbf{i}})r_{z\alpha}(\hat{\mathbf{i}})} & 0 \\ 0 & e^{i\Delta\kappa_{zq}(\hat{\mathbf{i}})r_{z\alpha}(\hat{\mathbf{i}})} \end{bmatrix} \quad (16)$$

where $\Delta\kappa_{zp}(\hat{\mathbf{i}})$ is defined in (8.b) and $r_{z\alpha} = |\mathbf{r}_\alpha \cdot \hat{\mathbf{n}}|$ is the vertical distance that the wave propagates within the mean medium. For direct paths from and to the particle (antennas in the real positions), they are given by $r_{z\alpha}(\hat{\mathbf{i}}_\alpha^-) = r_{z\alpha}(\hat{\mathbf{o}}_\alpha^+) = z_\alpha$, while for reflected paths from and to the particle (antennas in the image positions), they are given by $r_{z\alpha}(\hat{\mathbf{i}}_{\alpha I}^+) = r_{z\alpha}(\hat{\mathbf{o}}_{\alpha I}^-) = -z_\alpha + 2d$. Since each scattering mechanism follows a different path, the total path traveled will be different. The factors $B_{\alpha,n}^x$ in (12) that account for the spreading loss (r_{sr}/r_o) and path-dependent phase terms for each mechanism are thus unique. The magnitude of these ratios could deviate from 1 when the receiver is closer to vegetation. In other words, vegetation depth relative to the receiver height determines the significance of this factor. They are given by

$$B_{\alpha,n}^{dd} = \left(\frac{e^{ik_0(r_i+r_o)}}{r_i r_o} \right) / \left(\frac{e^{ik_0(r_{st}+r_{sr})}}{r_{st} r_{sr}} \right) \quad (17.a)$$

$$B_{\alpha,n}^{dr} = \left(\frac{e^{ik_0(r_{il}+r_o)}}{r_{il} r_o} \right) / \left(\frac{e^{ik_0(r_{st}+r_{sr})}}{r_{st} r_{sr}} \right) \quad (17.b)$$

$$B_{\alpha,n}^{rd} = \left(\frac{e^{ik_0(r_i+r_{ol})}}{r_i r_{ol}} \right) / \left(\frac{e^{ik_0(r_{st}+r_{sr})}}{r_{st} r_{sr}} \right) \quad (17.c)$$

$$B_{\alpha,n}^{rr} = \left(\frac{e^{ik_0(r_{il}+r_{ol})}}{r_{il} r_{ol}} \right) / \left(\frac{e^{ik_0(r_{st}+r_{sr})}}{r_{st} r_{sr}} \right) \quad (17.d)$$

Fig. 5 illustrates the directions of incoming and outgoing waves at an individual particle (i.e., a vertical trunk).

The polarization basis vectors, defined at the particle, differ for each direction due to the beam divergence. As a result, four distinct polarization rotation matrices have to be constructed. Following the procedure in Appendix B, the rotation matrices from the particle to the receiver (denoted by the subscript $p \rightarrow r$) are obtained as:

$$\underline{\underline{u}}_{p \rightarrow r}(\hat{\mathbf{o}}_a^+) = \begin{bmatrix} \hat{\mathbf{v}}_o^+ \cdot \hat{\mathbf{u}}_{r1}^* & \hat{\mathbf{h}}_o^+ \cdot \hat{\mathbf{u}}_{r1}^* \\ \hat{\mathbf{v}}_o^+ \cdot \hat{\mathbf{u}}_{r2}^* & \hat{\mathbf{h}}_o^+ \cdot \hat{\mathbf{u}}_{r2}^* \end{bmatrix} \quad \text{for } x = \text{dd, dr} \quad (18.a)$$

$$\underline{\underline{u}}_{p \rightarrow r}(\hat{\mathbf{o}}_{aI}^-) = \begin{bmatrix} \hat{\mathbf{v}}_{oI}^- \cdot \hat{\mathbf{u}}_{r1}^* & \hat{\mathbf{h}}_{oI}^- \cdot \hat{\mathbf{u}}_{r1}^* \\ \hat{\mathbf{v}}_{oI}^- \cdot \hat{\mathbf{u}}_{r2}^* & \hat{\mathbf{h}}_{oI}^- \cdot \hat{\mathbf{u}}_{r2}^* \end{bmatrix} \quad \text{for } x = \text{rd, rr} \quad (18.b)$$

and the rotation matrices from the transmitter to the particle (denoted by the subscript $t \rightarrow p$) are obtained as

$$\underline{\underline{u}}_{t \rightarrow p}(\hat{\mathbf{i}}_a^-) = \begin{bmatrix} \hat{\mathbf{u}}_{t1} \cdot \hat{\mathbf{v}}_{iI}^{-*} & \hat{\mathbf{u}}_{t2} \cdot \hat{\mathbf{v}}_{iI}^{-*} \\ \hat{\mathbf{u}}_{t1} \cdot \hat{\mathbf{h}}_{iI}^{-*} & \hat{\mathbf{u}}_{t2} \cdot \hat{\mathbf{h}}_{iI}^{-*} \end{bmatrix} \quad \text{for } x = \text{dd, rd} \quad (18.c)$$

$$\underline{\underline{u}}_{t \rightarrow p}(\hat{\mathbf{i}}_{aI}^+) = \begin{bmatrix} \hat{\mathbf{u}}_{t1} \cdot \hat{\mathbf{v}}_{iI}^{+*} & \hat{\mathbf{u}}_{t2} \cdot \hat{\mathbf{v}}_{iI}^{+*} \\ \hat{\mathbf{u}}_{t1} \cdot \hat{\mathbf{h}}_{iI}^{+*} & \hat{\mathbf{u}}_{t2} \cdot \hat{\mathbf{h}}_{iI}^{+*} \end{bmatrix} \quad \text{for } x = \text{dr, rr}. \quad (18.d)$$

The local horizontal (parallel to local $x'y'$ plane) and vertical polarizations for each direction are given by

$$\hat{\mathbf{h}}_o^+ = \frac{\hat{\mathbf{n}} \times \hat{\mathbf{o}}_a^+}{|\hat{\mathbf{n}} \times \hat{\mathbf{o}}_a^+|} \quad \text{and} \quad \hat{\mathbf{v}}_o^+ = \hat{\mathbf{h}}_o^+ \times \hat{\mathbf{o}}_a^+ \quad (19.a)$$

$$\hat{\mathbf{h}}_{oI}^- = \frac{\hat{\mathbf{n}} \times \hat{\mathbf{o}}_{aI}^-}{|\hat{\mathbf{n}} \times \hat{\mathbf{o}}_{aI}^-|} \quad \text{and} \quad \hat{\mathbf{v}}_{oI}^- = \hat{\mathbf{h}}_{oI}^- \times \hat{\mathbf{o}}_{aI}^- \quad (19.b)$$

$$\hat{\mathbf{h}}_i^- = \frac{\hat{\mathbf{i}}_a^- \times \hat{\mathbf{n}}}{|\hat{\mathbf{i}}_a^- \times \hat{\mathbf{n}}|} \quad \text{and} \quad \hat{\mathbf{v}}_i^- = \hat{\mathbf{i}}_a^- \times \hat{\mathbf{h}}_i^- \quad (19.c)$$

$$\hat{\mathbf{h}}_{iI}^+ = \frac{\hat{\mathbf{i}}_{aI}^+ \times \hat{\mathbf{n}}}{|\hat{\mathbf{i}}_{aI}^+ \times \hat{\mathbf{n}}|} \quad \text{and} \quad \hat{\mathbf{v}}_{iI}^+ = \hat{\mathbf{i}}_{aI}^+ \times \hat{\mathbf{h}}_{iI}^+ \quad (19.d)$$

4) *Received Power*: The total power received can be written in terms of the coherency vector as

$$\underline{\underline{P}}_T = \underline{\underline{b}} \otimes \underline{\underline{b}}^* \quad (20)$$

where $\underline{\underline{b}}^*$ is conjugate of $\underline{\underline{b}}$ and the operator \otimes indicates an outer product (Kronecker product) that is defined in Appendix D. Under the assumption that the scattering process is stationary and that the direct and multipath component fields arriving at the antennas from different directions are uncorrelated [45], the total power can be split into three independent terms as

$$\underline{\underline{P}}_T = \underline{\underline{P}}_d + \underline{\underline{P}}_m^{\text{coh}} + \underline{\underline{P}}_m^{\text{inc}} \quad (21.a)$$

where

$$\underline{\underline{P}}_d = \left\{ \frac{|K|^2}{r_d^2} \right\} \underline{\underline{D}} \quad (21.b)$$

$$\underline{\underline{P}}_m^{\text{coh}} = \left\{ \frac{|K|^2}{(r_{st} + r_{sr})^2} \right\} \underline{\underline{\Gamma}}_s \quad (21.c)$$

$$\underline{\underline{P}}_m^{\text{inc}} = \left\{ \frac{|K|^2 A_S}{4\pi r_{st}^2 r_{sr}^2} \right\} \underline{\underline{\sigma}}_e^0 \quad (21.d)$$

where

$$\underline{\underline{D}} = \underline{\underline{G}}_r(\hat{\mathbf{k}}_d) \cdot \underline{\underline{U}}_{t \rightarrow r}(\hat{\mathbf{k}}_d) \cdot \underline{\underline{G}}_t(\hat{\mathbf{k}}_d) \cdot \underline{\underline{E}}_t \quad (22.a)$$

$$\underline{\underline{\Gamma}}_s = \underline{\underline{G}}_r(\hat{\mathbf{o}}_s^+) \cdot \underline{\underline{U}}_{s \rightarrow r}(\hat{\mathbf{o}}_s^+) \cdot \underline{\underline{R}}_s(\hat{\mathbf{o}}_s^+, \hat{\mathbf{i}}_s^-) \cdot \underline{\underline{U}}_{t \rightarrow s}(\hat{\mathbf{i}}_s^-) \cdot \underline{\underline{G}}_t(\hat{\mathbf{i}}_s^-) \cdot \underline{\underline{E}}_t \quad (22.b)$$

$$\underline{\underline{\sigma}}_e^0 = \frac{1}{A_S} \sum_{\alpha} \sum_{n=1}^{N_{\alpha}} \sum_x |B_{\alpha,n}^x|^2 \times [\underline{\underline{G}}_r(\hat{\mathbf{o}}_x) \cdot \underline{\underline{U}}_{p \rightarrow r}^x(\hat{\mathbf{o}}_x) \cdot \underline{\underline{\sigma}}_{\alpha,n}^x(\hat{\mathbf{o}}_x, \hat{\mathbf{i}}_x) \cdot \underline{\underline{U}}_{t \rightarrow p}^x(\hat{\mathbf{i}}_x) \cdot \underline{\underline{G}}_t(\hat{\mathbf{i}}_x) \cdot \underline{\underline{E}}_t] \quad (22.c)$$

where four-by-one vectors, such as the coherency vector $\underline{\underline{P}}_T$, are written using uppercase letters and a single underline while four-by-four matrices are written using uppercase letters and a double underline. The coherency vectors $\underline{\underline{D}}$, $\underline{\underline{\Gamma}}_s$, and $\underline{\underline{\sigma}}_e^0$ represent direct signal, specular reflectivity, and “effective” normalized bistatic radar cross section (NBRCS), respectively. Note that antenna effects (e.g., the antenna beamwidths, polarization crosstalk, loss, and altitude) are incorporated into NBRCS (or bistatic scattering coefficient), which should represent the object scattering properties only. The expression in (22.c) is thus called “effective” NBRCS or $\underline{\underline{\sigma}}_e^0$ and also indicated with subscript e . The effects of system parameters on NBRCS will be examined in the simulation section.

In calculating the outer products, the following identity is utilized $(\underline{\underline{m}} \cdot \underline{\underline{n}}) \otimes (\underline{\underline{m}} \cdot \underline{\underline{n}})^* = (\underline{\underline{m}} \otimes \underline{\underline{m}}^*) \cdot (\underline{\underline{n}} \otimes \underline{\underline{n}}^*)$ and the following vectors/matrices are defined.

The coherency vector of transmit antenna polarization state is given by

$$\underline{\underline{E}}_t = \underline{\underline{e}}_t \otimes \underline{\underline{e}}_t^* \quad (23)$$

The antenna normalized (power) pattern matrices are given for the receive and transmit antennas, respectively, by

$$\underline{\underline{G}}_r = \underline{\underline{g}}_r \otimes \underline{\underline{g}}_r^* \quad (24.a)$$

$$\underline{\underline{G}}_t = \underline{\underline{g}}_t \otimes \underline{\underline{g}}_t^* \quad (24.b)$$

The polarization basis rotation matrices that operate on intensities are given by

$$\underline{\underline{U}}_{t \rightarrow r} = \underline{\underline{u}}_{t \rightarrow r} \otimes \underline{\underline{u}}_{t \rightarrow r}^* \quad (25.a)$$

$$\underline{\underline{U}}_{s \rightarrow r} = \underline{\underline{u}}_{s \rightarrow r} \otimes \underline{\underline{u}}_{s \rightarrow r}^* \quad (25.b)$$

$$\underline{\underline{U}}_{t \rightarrow s} = \underline{\underline{u}}_{t \rightarrow s} \otimes \underline{\underline{u}}_{t \rightarrow s}^* \quad (25.c)$$

$$\underline{\underline{U}}_{p \rightarrow r}^x = \underline{\underline{u}}_{p \rightarrow r}^x \otimes \underline{\underline{u}}_{p \rightarrow r}^{x*} \quad (25.d)$$

$$\underline{\underline{U}}_{t \rightarrow p}^x = \underline{\underline{u}}_{t \rightarrow p}^x \otimes \underline{\underline{u}}_{t \rightarrow p}^{x*} \quad (25.e)$$

In (22.b), the specular reflectivity operator that describes the scattering from the specular point is defined as

$$\underline{\underline{R}}_s = \underline{\underline{r}}_s \otimes \underline{\underline{r}}_s^* \quad (26)$$

In (22.c), A_S is the surface area that is limited to a few Fresnel zones to capture most of the contributions and may differ from the whole area projected by the receiver antenna. In space borne geometries, the relative area (discriminated by both Doppler and Delay) are small and system parameters are uniform within that area. However, as demonstrated in

Section II-B, as the receiver gets closer to the ground (low altitudes), the system parameters and size of the surface area get significant in NBRCS calculations. The formulation in (22.c) provides explicit expressions to correct the measured NBRCS by a ground-based system from the system-induced effects to be used in spaceborne data interpretation.

Finally, the bistatic scattering cross-section operator is given by

$$\underline{\underline{\sigma}}_{\alpha,n}^x = 4\pi \left[\underline{\underline{s}}_{\alpha,n}^x \otimes \underline{\underline{s}}_{\alpha,n}^{x*} \right]. \quad (27)$$

B. Special Case ($r_{st} \gg r_{sr}$)

The expressions given above [namely, (21)] do not impose any restriction on the relative distance between receiver and transmitter slant ranges except that both transmitter and receiver are in the far field of each other and both of them are in the far-zone of vegetation constituents above ground. On the other hand, in SoOp studies for remote sensing of earth properties, the utilized transmitters are mostly located in medium earth orbit (MEO) such as GNSS or geostationary orbit (GEO) such as communication satellites, and the receivers are operated from different platforms: ground, airborne, or spaceborne at low earth orbit. For all of these scenarios, the relative distance between transmitter and receivers to the specular point is large, i.e., $r_{st} \gg r_{sr}$. By taking advantage of this large difference, a flat earth approximation around the specular point can be applied. Moreover, for the transmitters at MEO and GEO, the range from the transmitter to the ground and the incidence angle direction can be assumed to be equal for all the surface surrounding the specular point. The footprint associated with Fresnel zones can be approximated with the following semiminor and semimajor axes, respectively, [46]:

$$b = \frac{\sqrt{2\delta_n h_r \cos \theta_s}}{\cos \theta_s} \quad (28.a)$$

$$a = \frac{b}{\cos \theta_s} \quad (28.b)$$

where θ_s is the angle of reflection at the specular point as defined in (7), h_r is the receiver height with respect to ground, $\delta_n = n\lambda_0/2$ defines iso-delay ellipsis with the delay of multiples of half-wavelengths, and n is the Fresnel zone number. The n th Fresnel zone is defined as the surface between the n th and $(n-1)$ th ellipsis. Even though one can use the exact expression for Fresnel ellipses given in [31], the above expressions remain fairly accurate for most practical cases [47] and provide a better physical grasp of the footprint. The reflected GNSS signal mainly comes within the first ($n = 1$) Fresnel zone over land unless topographic effects are present as indicated in [3] while the reflected signals over ocean emanate over the multiple Fresnel zones (Glistening zone) [46]. It is important to identify contributing Fresnel zones and the scattering mechanism not only to determine the footprint but also to arrive at a physical model that is suitable for inversion.

The reflected signals are generally a superposition of both the coherent (specular), incoherent (diffuse) scattering, and direct components as given in (21). For down-looking antennas, the direct signal can be significantly suppressed, but the

question remains on the relative importance of coherent and incoherent contributions over land with respect to platform altitude. It is important to recognize the path loss dependence with distance of each term. The specularly reflected signal follow a total ray path dependence, i.e., $1/(r_{st}+r_{sr})^2$ due to the image theory, while the diffuse term exhibits a multiplicative dependence given by $1/(r_{st}^2 r_{sr}^2)$ due to the additional spreading loss, the incident signal experiences after reradiation from the vegetation scatterers. The diffuse term thus decreases more rapidly with distance than the specular component. These differences are manifested in the relative weights of these two components for different receiving platforms: ground, airborne, and spaceborne.

Let us assume that specular reflection is dominant over land and find out how much diffuse scattering alters the specular reflectivity as a function of altitude. By normalizing the total power \underline{P}_T with $|K|^2/(r_{st} + r_{sr})^2$, approximating the surface area ($= \pi ab$) with (28), and neglecting the direct contribution, the reflectivity of the total reflected signal $\underline{\Gamma}_s^{(T)}$ can be obtained

$$\underline{\Gamma}_s^{(T)} \cong \underline{\Gamma}_s + \left(\frac{\delta_n}{2h_r} \right) \underline{\sigma}_e^0 \quad (29)$$

where the specular reflectivity $\underline{\Gamma}_s$ and the effective NBRCS $\underline{\sigma}_e^0$ are given in (22). The second term represents the contribution to reflectivity of incoherent scattering from the first “ n ” Fresnel zones. It is clear that the relative contribution of the NBRCS (diffuse contribution) is inversely proportional to the receiver altitude (h_r). This indicates that the specular component contains a greater portion of the total energy and thus contributes more to the received power unless: 1) NBRCS is significantly larger than specular reflectivity; 2) more Fresnel zones contribute; 3) the receiver is located at close neighborhood of the ground; or 4) any combination of the above cases happens. Diffuse scattering, although weak at high altitude, can have significant influence on ground and airborne systems which are usually used as a testbed for algorithm development for spaceborne missions. In addition, the reflected signals could still include significant incoherent scattering components and the relative importance of these contributions is expected to vary with respect to the scene properties around the specular point. For these reasons, the diffuse component should be included in the model for low-altitude platforms. A bistatic model based solely on image theory cannot account for diffusely scattering.

III. NUMERICAL RESULTS AND DISCUSSION

The SCoBi-Veg model considers single scattering so it is intrinsically valid at P-, L-, and S-bands. There are already many potential free illuminators within these frequency ranges that could be used for earth science applications. Furthermore, the model could be extended to exploit signals at other bands if multilayer soil for lower frequencies or multiple scattering for higher frequencies are included. The particular communication satellites of interests to the recent studies [20]–[22] are the Navy’s Mobile Users Objective System (MUOS) operating with RHCP transmit signals at P-band frequencies (360–380 and 240–270 MHz). There are four MUOS

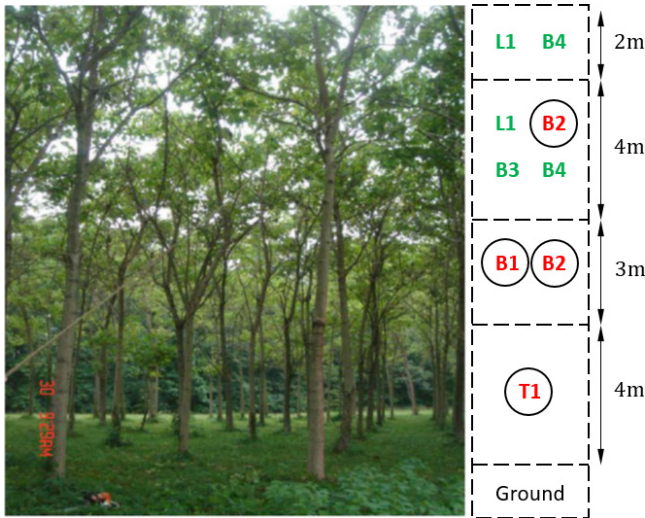


Fig. 6. (Left) Paulownia stands [48]. (Right) Distributions of scatterers are illustrated. The scatterer kinds that are indicated by circles are primary branches or trunks that contribute the scattering while the others contribute the attenuation only. Canopy parameters are provided in Table I.

satellites at geostationary altitudes ($\sim 32\,810$ km), providing global coverage, except near the polar cap. As a preliminary application of the model, we will limit ourselves to P-band (370 MHz). The purpose of the simulations is twofold: 1) to show physical relevance of the model behavior to the SoOp studies in general and 2) to provide insights into polarimetric aspects of specular and diffuse contributions at P-band for a tree canopy observed from platforms at various altitudes.

The model requires various soil and vegetation parameters as inputs. In this paper, we will use the *in situ* parameters collected in an active/passive soil moisture experiment in Maryland in 2006 [48]. The experimental site consisted of plots of planted stands of deciduous Paulownia trees, a fast-growing deciduous tree with broad leaves shown in Fig. 6. The tree plot used in this paper had 92 trees in a 1089-m^2 area. The dry biomass was about 9 kg/m^2 , while the woody volume and density were $185.8\text{ m}^3/\text{ha}$ and 477.6 kg/m^3 , respectively. The diameter at breast height (DBH) ranged from 17 to 23 cm (average DBH = 19.4 cm). The tree heights were variable, on the order of 11–14 m (average height = 13 m). Detailed measurements of the size/angle distributions of the tree constituents (trunk, branches, and leaves), along with their densities, were made. The results from the canopy sampling and dielectric measurements are shown in Table I. Clear boundaries within canopy and trunk layers were identified by visual inspection. Fig. 6 (right) shows the distribution of vegetation components within the vegetation layers. The soil texture at the site was a loamy sand, consisting of 80% sand and 7% clay. The ground was flat with a relatively smooth surface, where the surface rms height was on the order of 0.5–1 cm.

A. Simulation Setting

The model considers both specular and diffuse scattering by incorporating the statistical and physical properties of

TABLE I
CANOPY PARAMETERS FROM DESTRUCTIVE SAMPLING [48]

Constituents		Average Parameters				
Types	Kinds	Length [cm]	Radius [cm]	Density [m^{-3}]	Dielectric Constant	Orientation Uniform
Trunks	T1	617.0	8.73	0.005	15.6+i3.8	Vertical
Primary Branches	B1	187.0	4.30	0.016	12.0+i2.9	$20^\circ - 50^\circ$
	B2	153.8	1.58	0.188	12.0+i2.9	$10^\circ - 60^\circ$
Secondary Branches	B3	63.6	0.98	0.734	12.0+i2.9	$0^\circ - 90^\circ$
	B4	48.1	0.45	1.933	12.0+i2.9	$0^\circ - 90^\circ$
Leaves	L1	Thickness 0.012	10.2	11.12	35.2+i5.3	$0^\circ - 90^\circ$

the terrain into the received signal. While the calculation of the specular term requires properties of the mean vegetation attenuation in one direction and soil parameters at a single point, the diffuse term involves contributions of various scattering mechanisms due to each particle within the illuminated volume. In this present investigation, a Monte Carlo procedure is chosen to predict the bistatic diffuse response from vegetation. Monte Carlo simulations are very useful to incorporate coherent addition and wave interaction effects in a vegetation canopy. The scheme holds possibility to incorporate realistic canopy structures such as architectural plant model [49], experimental vectorization [38], or recursive Lindenmayer systems [50] due to its generic model formulation. However, the base vegetation module in SCoBi-Veg is restricted for the moment to use a simple multilayer canopy model where the scatterers are spread uniformly between illuminated layers using a given distribution. Due to the single-scattering assumption, the scatterers are assumed to be independent and no mutual interactions are considered.

The scattering contributions of electrically large components only [e.g., primary branches (B1, B2) and trunks (T1)] are considered in order to speed up the computation while the calculation of the mean medium involves attenuation due to all scatterers. Scattering due to leaves (L1) and secondary branches (B3 and B4) is ignored since their dimensions are much smaller than the wavelength (81 cm) at P-band. The number of significant scatterers is calculated within the Fresnel zones based on their particle densities (see Table I). They are then embedded in the equivalent (mean) medium where random positions are generated for these scatterers in the illuminated volume based on their associated layers as indicated in Fig. 6; each scatterer is then oriented according to some prescribed orientation statistics given in Table I. The solutions of the bistatic electric fields are computed for each particle by combining the configuration attributes, bistatic scattering amplitude from each significant scatterers, and ground reflection; these are then summed coherently. Finally, by repeating for many realizations of the random medium, the average received field of the bistatic scattered field is obtained from the responses averaged over all realizations. We found that 20 realizations for 20–100-m altitudes and 10 realizations for 500-m altitude provided sufficient convergence in the diffuse term results. As the altitude increases, the required number of

realization for good convergence gets reduced since the larger footprint size already adds randomness to the scattering at higher altitudes.

Over the years, various observing strategies have been developed for SoOp studies, mostly GNSS-R applications. These include the following:

- 1) geodetic ground-based nearly hemispherical RHCP antenna [10];
- 2) horizontal-pointing vertically polarized antenna [7];
- 3) down-looking LHCP antenna and an up-looking RHCP antenna [51];
- 4) one RHCP up-looking antenna and two down-looking antennas with one RHCP polarized and the other LHCP polarized [9];
- 5) a two-element dual linearly polarized patch array mounted side of an aircraft by steering a null to the direction of the undesired signal [21].

The model can handle any configuration stated above or more general configuration where vertically and horizontally polarized antennas for both the up- and down-looking. In the present investigation, we are, however, going to restrict the simulations to situation where the dual circularly polarized receiver antenna (both RHCP and LHCP) points directly to the specular point to understand the angular dependence of polarimetric reflected signatures. In other words, both transmitter and receiver are configured such that both are pointing to the specular point ($\theta_i = \theta_s$) for the simulations provided below. Furthermore, no Doppler frequency shifts are considered due to geostationary transmitters and low-altitude receiver assumptions considered in the present setup.

A generalized Gaussian antenna pattern, including 25-dB sidelobes, 25-dB crosstalk, and 30° beamwidth (arbitrary values), is assumed as an approximation to the radiation pattern needed in this formulation. This pattern will be assumed to be circularly symmetrical about the direction of peak intensity. In the following simulations, both a receiving antenna gain and EIRP equal to 0 dB were supposed. The actual values depend on the choice of illuminator, actual receiver antenna, and processing gain. They affect the received power in dB only by an offset and do not change its sensitivity to the reflected signature.

B. Results and Discussion

For most SoOp scenarios, it is assumed that only coherent scattering takes place over land, so the incoherent component is neglected. This assumption relies only on the specular scattering driven by the Fresnel reflection coefficients. On the other hand, the reflected signals are generally a combination of both the coherent (specular) and incoherent (diffuse) scattering components. In Fig. 7, a comparison is presented between diffuse (the filled circle marker) and specular (the filled square marker) contributions over Paulownia trees as a function of observation angle (θ_s) at various receiver heights (20, 50, 100, and 500 m). Fig. 7 (left) shows cross-polarized (RL—RHCP transmit, LHCP receive) received power while Fig. 7 (right) shows co-polarized (RR—RHCP transmit, RHCP receive) received power. In Fig. 7, the results of specular reflection

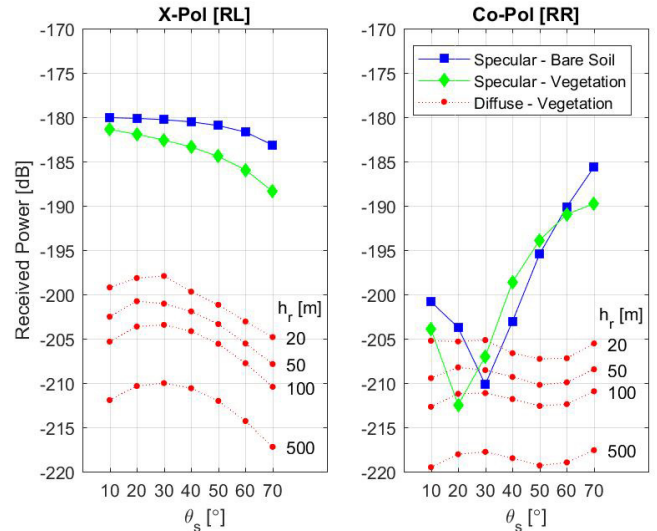


Fig. 7. Relative contributions of coherent and incoherent components of received power as a function of incidence angle and the receiver altitude. (Left) cross-polarization (RL) received power. (Right) Co-polarization (RR) received power. Both receiver gain and EIRP were set to 0 dB. The received power will shift up with actual system EIRP, receiver gain, and processing gains (coherent/incoherent integrations).

from a bare soil are also added and are represented by filled diamond marker. As it can be seen, as the receiver altitude increases from 20 to 500 m, the diffuse term in both polarization is greatly reduced due to multiplicative dependence of path loss of the diffuse term [see (21.d)] and the specular term remains the same since its path loss has a total path ray dependence [see (21.c)] and the receiver altitude is much smaller than the GEO satellite altitudes. Similar results were experimentally observed by a GNSS-R balloon experiment where the received power did not change with the balloon height [13], indicating that the coherent term dominates the received signal.

It is evident from the results in Fig. 7 that the cross-polarized coherent term will always dominate the received power even for the receiver at low altitudes for flat terrains (i.e., in the absence of topographic relief) and cross-polarized diffuse term can thus be ignored. Similar result for cross-polarized reflected GNSS signals has been confirmed by spaceborne observations at L-band [3]. On the other hand, co-polarized diffuse term could be comparable or even larger than co-polarized specular term at lower incidence angles and low altitudes. As the incidence angle increases, co-polarized specular term starts to overpass the diffuse term again. This indicates that the reflected co-polarized signals could still include incoherent scattering components at low altitudes and the relative importance of these contributions is expected to vary with respect to the scene properties around the specular point and incidence angle. This has important implications for studies that use the co- and cross-polarization power ratio [9] to cancel out common factors and to make soil moisture inversion more robust against roughness. The diffuse contributions for low-altitude observations should be included in the model and interpretation of the results since both specular and diffuse

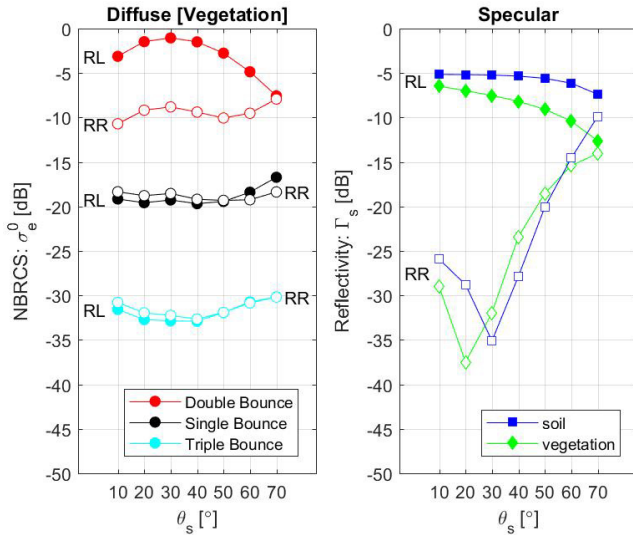


Fig. 8. (Left) Angular responses of NBRCS scattering mechanisms and (Right) specular reflectivity. The filled markers denote cross-polarization (RL) while the unfilled markers represent co-polarization (RR). The receiver altitude is 500 m and the first Fresnel response is considered.

terms have different dependence on the path loss, polarization, and incidence angle.

The diffuse scattering includes volume scattering within canopy, double bounce effects due to soil and trunk/canopy interactions, as well as attenuation by the vegetation canopy. Fig. 8 provides comparison between specular reflectivity of bare soil (square marker) and vegetation (diamond marker), and effective NBRCSs (circular markers) of diffuse scattering mechanisms. It is well-known that ground reflection changes its circular polarization from right hand to left hand and vice versa. The cross-polarization specular reflectivity is thus much higher than co-polarization reflectivity at low incidence angles and both responses merge as the angle approaches Brewster angle as shown in Fig. 8 (right). At lower incidence angles, the RR-polarized specular reflectivity first goes down and picks up again around 20°–30°. This behavior (same in Fig. 7) happens due to the crosstalk (25 dB in this investigation) between the receiving antenna ports which makes a fraction of the signal go into the opposite polarization port. Furthermore, the cross-polarization specular responses of both bare soil and vegetation show a decreasing trend with increasing angle of observation, but the drop in vegetation reflectivity is more substantial due to the increasing attenuation by the plant canopy with increasing incidence angle.

In Fig. 8 (left), the effective NBRCS is decomposed into its scattering mechanisms: single bounce, double bounce, and triple bounce. The single bounce shows no difference between cross- and co-polarized signatures since it involves no ground reflection and the volume scattering does not have any preference for circular polarization handedness. Similarly, the triple bounce shows no polarization difference either since the wave bounces twice from the ground. The first bounce changes RHCP to LHCP and the second bounce changes back to the RHCP. The triple bounce is also the smallest contribution due to double ground reflection. On the other

hand, the double bounce response produces the largest among the other mechanisms since it bounces once from the ground and its scattering angle is well aligned with vertical trunks' scattering cones, where the amplitude of the scattering has its maximum in a conical region [52].

There are some remarkable features in both polarimetric and angular response of NBRCS. First, the cross-polarization NBRCS of the double-bounce contribution is higher than co-polarization NBRCS at low incidence angles and both response merges at higher angles. This is similar to the specular reflectivity response as described above, but the polarization difference is much smaller in NBRCS since volume scattering within vegetation combines two polarized components and reduces their relative strength. This difference is also much smaller than the present antenna crosstalk, which is 25 dB. This indicates that polarization mixing due to vegetation scattering is the main cause of this behavior. Second, cross-polarization NBRCS response shows an increasing trend up to $\sim 30^\circ$ incidence angle, and then decreases with increase in the incidence angle in contrast to the cross-polarization specular reflectivity that always decreases with the incidence angle.

Note that the both specular reflectivity and NBRCS of the vegetation depend not only on the surface and vegetation parameters but also on system parameters such as the receiving and transmitting antenna parameters, and altitude. In Fig. 9, the effect of the receiver altitude on the diffuse term is further investigated by including the antenna characteristics and Fresnel zones by using expression in (22.c) that provides the explicit dependence of NBRCS on the system parameters. In Fig. 9(a), effective NBRCS is plotted against the number of Fresnel zones at various heights for ideal (nonfilled markers) and beam-limited (filled markers) antennas. The left panel shows cross-polarized (RL) NBRCS while the right panel shows co-polarized (RR) NBRCS. As can be seen from Fig. 9, it is clear that: 1) in both polarization, effective NBRCS decreases as more Fresnel zones are included; 2) higher effective NBRCS is observed with higher altitudes; and 3) at lower altitudes, antenna radiation pattern plays a greater role in NBRCS values. It can be clearly noticed that NBRCS, which should represent the scene scattering properties only, is blended with the system parameters, particularly at lower altitudes. Most of the current experimental studies are carried out from lower altitude platforms that are often used before spaceborne implementation. In order to link these studies to spaceborne observation, the system-related effects need to be corrected to arrive at scene-only NBRCS.

Fig. 9(b)–(d) shows the projection of the receiver antenna footprints and 10 Fresnel zones on the ground from 20, 50, 100, and 500 m observing altitudes to provide further insight into the system-related effects on NBRCS. As evident from Fig. 9(b)–(d), the relative area covered by the same number of Fresnel zones with respect to antenna footprint gets reduced as the altitude increases. As a result, the scattering angles are more confined around the boresight direction of the receiver antenna radiation pattern at higher altitudes. For instance, less decrease in NBRCS is observed at 500 m. When the results by using ideal (unit pattern matrix) and

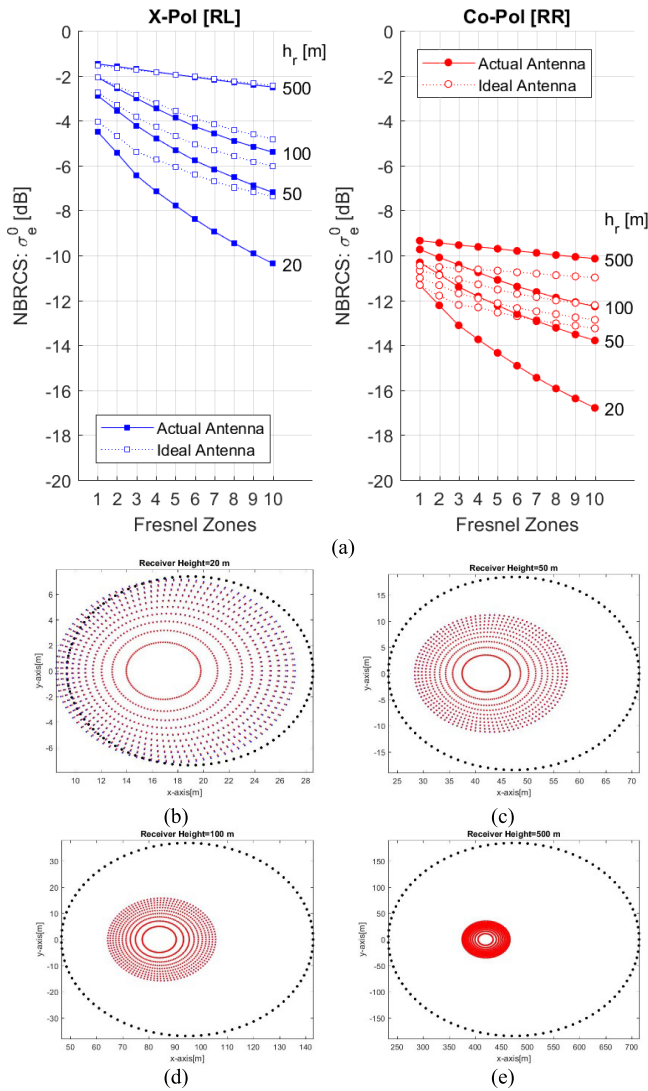


Fig. 9. (a) “Effective” NBRCS as a function of increasing Fresnel zones (from 1 to 10), which is cumulative and includes inner Fresnel zones at various heights for ideal (the nonfilled markers) and beam-limited (the filled markers) antennas. (b)–(e) Fresnel zones and projected antenna footprint on the ground for receivers at various heights. The red ellipses (total of 10) are Fresnel zones while the black ellipse is antenna footprint.

actual (beam-limited) antennas are compared, it is clear that even if we use pencil beam (ideal) antenna, the NBRCS still gets reduced as new Fresnel zones are included. This is due to the trunk’s unique scattering patterns, which scatter most in a conical region. The scattering angles are much more spread at lower altitudes as shown in Fig. 9(b)–(d). Due to the spread of the wave, different particles in the layer experience different scattering directions. The weaker scattered fields are observed in the bistatic direction associated with trunk-ground interaction since the scattered wave from vertical trunks becomes slightly away from the forward scattering cone as shown in Fig. 10(a). The amplitude of the scattering has its maximum in a conical region as illustrated in Fig. 10(b). It is sometimes called skirt as well. For electrically large cylinders, this cone is sharp. As the scattering direction moves away from specular/forward direction, the specular scattering gets reduced drastically. This scattering behavior of vertical trunks acts like

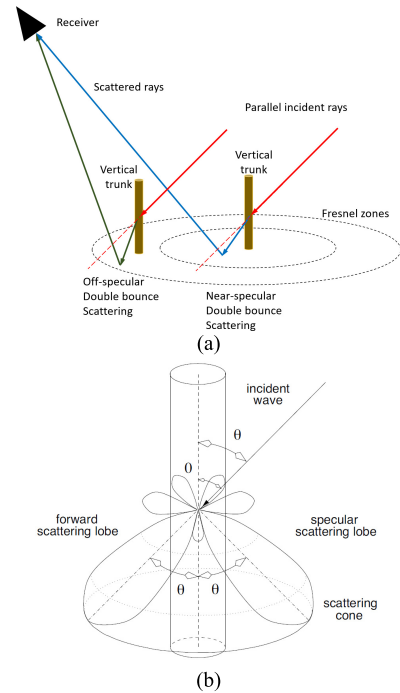


Fig. 10. (a) Effect of beam divergence on double bounce. (b) Scattering pattern of a vertical trunk [52, Fig. 4].

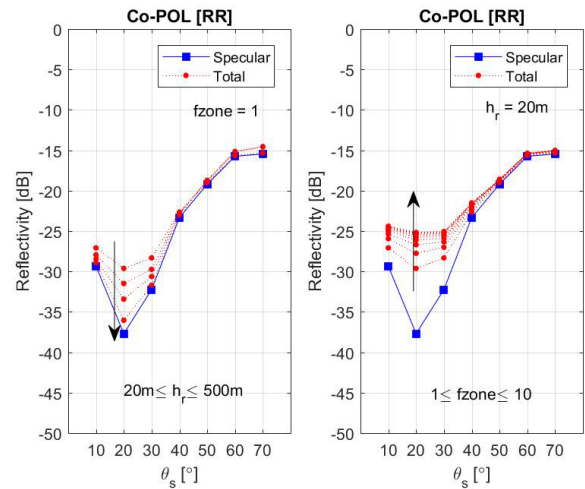


Fig. 11. Effect of diffuse contribution on the reflectivity of total reflected signal. (Left) While the arrow indicates increasing altitude (20–500 m) for the first Fresnel zone, (Right) arrow indicates increasing Fresnel zone indices (1–10), which is cumulative and includes inner Fresnel zones, at a receiver height of 20 m.

a special filter and concentrates most of the power along the specular direction since the local scattering angles get diverted from the specular directions for those that are located in higher Fresnel zones.

As stated earlier, the cross-polarization coherent scattering from vegetation over a flat ground almost always overpass the diffuse contribution to the received power. However, co-polarization diffuse power can be comparable or can be even larger than co-polarization coherent received power. It is worth investigating the effect of diffuse contribution on the co-polarization specular reflectivity. Fig. 11 shows the effect of diffuse contribution in the first Fresnel zone

as a function of altitude (left) and at 20-m altitude as a function of contributing Fresnel zones (right). The filled square marker represents specular reflectivity [(22.b)] while smaller filled circles denote reflectivity of total received signal (specular + diffuse) [see (29)]. As seen from Fig. 11 (left), as the altitude increases (increasing altitude is indicated by an arrow in Fig. 11), the total reflectivity approaches the specular reflectivity. The effect of diffuse scattering is more apparent at lower incidence angles. On the other hand, as more Fresnel zones are included (increasing Fresnel zones are indicated with an arrow in Fig. 11), the total reflectivity diverges from the specular reflectivity, particularly at lower incidence angles. This increase in the total reflectivity is due to additional diffuse scattering with more Fresnel zones. As a result, additional diffuse contributions to the total reflectivity will alter its angular signature as a function of both Fresnel zones and receiver height and may introduce errors on the estimation of well-known Fresnel reflection coefficients that are often used in soil moisture retrievals. Diffuse scattering, although weak at high altitude, can have significant influence on co-polarization reflectivity observed by ground and airborne systems which are usually used as a testbed for algorithm development for spaceborne missions. If co-polarized signals are used in the retrievals, the co-polarized diffuse component should be included in the model for low-altitude platforms such as tower or small UAS.

IV. CONCLUSION

There is increasing interest to use reflected (or multipath) navigation and communication satellite signals for remote sensing of a number of geophysical land parameters such as soil moisture and biomass. Although the handful experimental and theoretical studies demonstrate the potential of spaceborne SoOp observations for such applications, there are many unknowns regarding the impacts of vegetation and system parameters on the observations. The scattering models are thus a critical means in advancement of these studies and in the design of future missions or field campaigns. In this paper, we presented an overview of the newly formulated coherent bistatic vegetation model, i.e., SCoBi-Veg, which simulates polarimetric reflectometry of vegetated landscapes using a Monte Carlo scheme. The model calculates the complex field in direct, specular, and diffuse terms by explicitly accounting for both system parameters (e.g., the antenna beamwidth, polarization crosstalk, polarization mismatch, and altitude) and the statistical and physical properties of the terrain. In contrast to the previous studies that have usually assumed plane wave illumination/scattering, and/or ignored such antenna effects, the SCoBi-Veg model considers variations of both the strength and polarization states of the received wave along the beam direction so that the same model could be uniformly applied across different platforms at various altitudes.

P-band signals of geostationary communication satellites are considered as an application of the model. Although the results in this paper are not directly validated with experimental data and can be considered preliminary, simulated results provide insights into model's polarimetric and angular behavior with

respect to system and scene parameters. To illustrate usefulness of the model in interpretation of field data, we present in-depth analysis of polarimetric specular and diffuse contributions to bistatic scattering from tree canopies at P-band. First, the coherent and diffuse components of the reflected signatures from tree canopies are compared for down-looking dual circular polarized receivers at various altitudes. It is shown that the cross-polarized coherent term dominates the received power over flat vegetated terrains, but co-polarized diffuse term could be comparable or even larger than co-polarized specular term at lower incidence angles and low altitudes. Second, the diffuse scattering was decomposed into the scattering mechanisms and the double bounce was shown to be the main contributor. Furthermore, the double bounce from the vertical trunks acts like a special filter and concentrates most of the reflected power along the specular direction. Third, the effect of antenna beamwidth and altitude on the diffuse scattering was also quantified. It is shown that the NBRCS, which depends on the scene scattering properties only by definition, are blended with the system parameters, particularly at lower altitudes. Forth, even though the relative contribution of the NBRCS to the total reflectivity is inversely proportional to the receiver height, diffuse scattering can still alter angular signature of co-polarized reflectivity as a function of both Fresnel zones and receiver height. This may introduce errors on estimation of well-known Fresnel reflection coefficients that are often used in soil moisture retrievals. If co-polarized signals are used in the retrievals, the co-polarized diffuse component should be included in the model for low-altitude platforms and be corrected for antenna and altitude effects.

APPENDIX A

NORMALIZED "VOLTAGE" PATTERN

In this appendix, the normalized "voltage pattern" for both linear and circular polarization basis will be expressed. Due to reciprocity, the following arguments are equally applicable for antennas in transmit and receive modes.

In practice, antennas cannot be constructed to produce pure polarization states [37]. It is important to decompose the radiated field into two orthonormal polarization states. The orthogonal polarization states are commonly chosen along the linear or circular basis vectors. For linear basis, co-polarized and cross-polarized patterns are defined for each port as

$$\mathbf{g}_X = g_{XX}\hat{\mathbf{u}}_1^X + g_{XY}\hat{\mathbf{u}}_2^Y \quad (\text{A.1a})$$

$$\mathbf{g}_Y = g_{YX}\hat{\mathbf{u}}_1^X + g_{YY}\hat{\mathbf{u}}_2^Y \quad (\text{A.1b})$$

where g_{XX} is the co-polarized voltage pattern for port 1 while g_{XY} is the cross-polarized voltage pattern for the same port. The quantity g_{YY} is the co-polarized voltage pattern for port 2 while g_{YX} is the cross-polarized voltage pattern for the same port. The voltage patterns are complex. The cross-polarized patterns represent the crosstalk between antenna ports. The unit vectors $\hat{\mathbf{u}}_1^X$ and $\hat{\mathbf{u}}_2^Y$ are also complex and are associated with co-polarization and cross-polarization states.

In linear basis, the polarization vectors are chosen according to Ludwig's third definition of polarization to indicate the directions of co-polarization and cross-polarization [53]. They

are rotated versions of spherical vectors defined in antenna coordinates and can be written as

$$\hat{\mathbf{u}}_1^X = \cos \varphi \hat{\boldsymbol{\theta}} - \sin \varphi \hat{\boldsymbol{\phi}} \quad (\text{A.2a})$$

$$\hat{\mathbf{u}}_2^Y = \sin \varphi \hat{\boldsymbol{\theta}} + \cos \varphi \hat{\boldsymbol{\phi}} \quad (\text{A.2b})$$

where $\hat{\boldsymbol{\theta}}$ and $\hat{\boldsymbol{\phi}}$ are the unit vectors in spherical coordinates of the antenna. Thus, the normalized ‘‘voltage’’ pattern matrix for the linearly polarized antenna is given as

$$\underline{\underline{\mathbf{g}}} = \begin{bmatrix} g_{XX} & g_{XY} \\ g_{YX} & g_{YY} \end{bmatrix} \quad (\text{A.3})$$

For RHCP as the reference polarization and LHCP as the cross-polarization, the unit polarization vectors are

$$\hat{\mathbf{u}}_1^R = \frac{1}{\sqrt{2}}(\hat{\mathbf{u}}_1^X - i\hat{\mathbf{u}}_2^Y) \quad (\text{A.4a})$$

$$\hat{\mathbf{u}}_2^L = \frac{1}{\sqrt{2}}(\hat{\mathbf{u}}_1^X + i\hat{\mathbf{u}}_2^Y) \quad (\text{A.4b})$$

Similarly, for circular polarization basis, co-polarized and cross-polarized patterns can be written for each port as

$$\mathbf{g}_R = g_{RR}\hat{\mathbf{u}}_1^R + g_{RL}\hat{\mathbf{u}}_2^L \quad (\text{A.5a})$$

$$\mathbf{g}_L = g_{LR}\hat{\mathbf{u}}_1^R + g_{LL}\hat{\mathbf{u}}_2^L \quad (\text{A.5b})$$

where the subscripts/superscripts R and L denotes RHCP and LHCP, respectively. The normalized ‘‘voltage’’ pattern matrix for the circularly polarized antenna is given as

$$\underline{\underline{\mathbf{g}}} = \begin{bmatrix} g_{RR} & g_{RL} \\ g_{LR} & g_{LL} \end{bmatrix} \quad (\text{A.6})$$

where the diagonal elements are co-polarized patterns while the off-diagonal elements are cross-polarized patterns. The elements are all complex.

APPENDIX B

POLARIZATION BASIS TRANSFORMATION

An arbitrary-polarized electric field can always be expressed by a linear combination of two orthogonal (basis) fields that are usually defined in one coordinate system [54]. Since bistatic scattering involves radiation, scattering, and reception in various coordinate systems, it is necessary to transform polarization basis vectors in one coordinate system to another one. In this appendix, we will consider two configurations: transmit–receive and transmit–scattering–receive as depicted in Fig. 12.

A. Transmit–Receive Configuration

Let us first consider two arbitrary-oriented antenna coordinate systems that are denoted by $T : (x_t, y_t, z_t)$ and $R : (x_r, y_r, z_r)$ as shown in Fig. 12(a). The unit vectors $\hat{\mathbf{u}}_{r1}$ and $\hat{\mathbf{u}}_{r2}$ are complex orthonormal and defined in the transmit antenna system T while the unit vectors $\hat{\mathbf{u}}_{r1}$ and $\hat{\mathbf{u}}_{r2}$ are complex orthonormal and defined in the receive antenna system R . An arbitrary electrical field can be decomposed into orthogonal components in both systems as

$$\mathbf{E} = E_{t1}\hat{\mathbf{u}}_{t1} + E_{t2}\hat{\mathbf{u}}_{t2} \quad (\text{B.1a})$$

$$\mathbf{E} = E_{r1}\hat{\mathbf{u}}_{r1} + E_{r2}\hat{\mathbf{u}}_{r2} \quad (\text{B.1b})$$

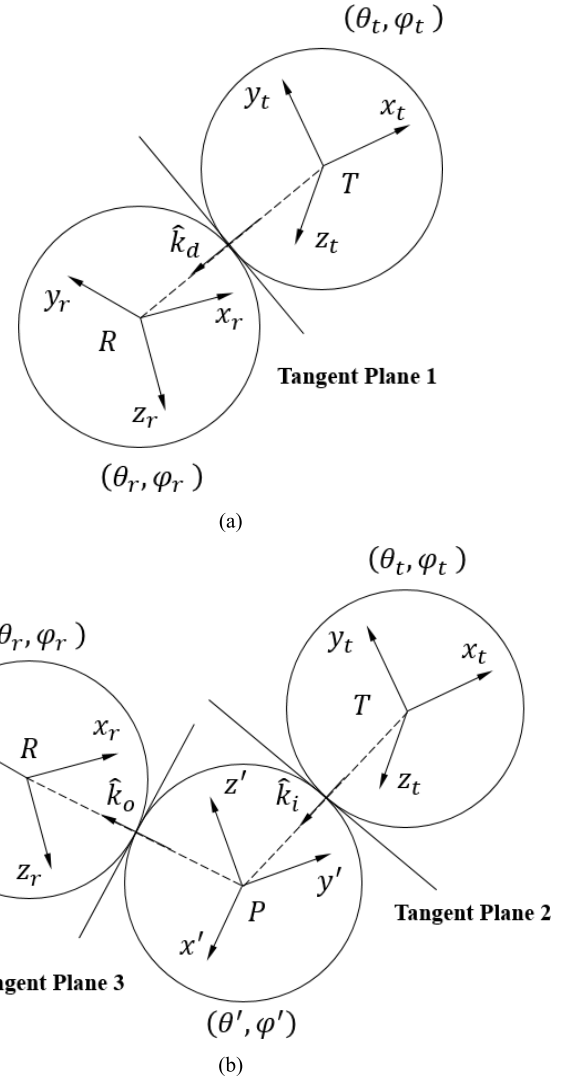


Fig. 12. Change of polarization basis (a) between transmitter and receiver and (b) between transmitter, ground, and receiver.

The components of the field in both coordinates are related as

$$E_{r1} = \mathbf{E} \cdot \hat{\mathbf{u}}_{r1}^* = E_{t1}(\hat{\mathbf{u}}_{t1} \cdot \hat{\mathbf{u}}_{r1}^*) + E_{t2}(\hat{\mathbf{u}}_{t2} \cdot \hat{\mathbf{u}}_{r1}^*) \quad (\text{B.2a})$$

$$E_{r2} = \mathbf{E} \cdot \hat{\mathbf{u}}_{r2}^* = E_{t1}(\hat{\mathbf{u}}_{t1} \cdot \hat{\mathbf{u}}_{r2}^*) + E_{t2}(\hat{\mathbf{u}}_{t2} \cdot \hat{\mathbf{u}}_{r2}^*) \quad (\text{B.2b})$$

The above equations can be cast into a matrix form as

$$\begin{bmatrix} E_{r1} \\ E_{r2} \end{bmatrix} = \underline{\underline{\mathbf{u}}}_{t \rightarrow r} \begin{bmatrix} E_{t1} \\ E_{t2} \end{bmatrix} \quad (\text{B.3a})$$

where the transformation matrix $\underline{\underline{\mathbf{u}}}_{t \rightarrow r}$ is given by

$$\underline{\underline{\mathbf{u}}}_{t \rightarrow r} = \begin{bmatrix} \hat{\mathbf{u}}_{t1} \cdot \hat{\mathbf{u}}_{r1}^* & \hat{\mathbf{u}}_{t2} \cdot \hat{\mathbf{u}}_{r1}^* \\ \hat{\mathbf{u}}_{t1} \cdot \hat{\mathbf{u}}_{r2}^* & \hat{\mathbf{u}}_{t2} \cdot \hat{\mathbf{u}}_{r2}^* \end{bmatrix} \quad (\text{B.3b})$$

where it transforms polarization components of the system T to those in the system R . The matrix is, in fact, a unitary matrix that conserves the total power of a wave, that is, the norm of the electric field vector remains invariant under change of basis [54]. As a result, the inverse of the transformation matrix (or transformation from R to T) is

$$\underline{\underline{\mathbf{u}}}_{r \rightarrow t} = \underline{\underline{\mathbf{u}}}_{t \rightarrow r}^{-1} = \underline{\underline{\mathbf{u}}}_{t \rightarrow r}^H \quad (\text{B.4})$$

where superscript -1 and H are the inverse and the Hermitian (or conjugate) transpose of a matrix, respectively.

Now let us consider the unit spherical vectors (orthogonal sets) in both coordinate systems. The direction of propagation is denoted by $\hat{\mathbf{k}}_d$ vector that connects origins of both coordinate systems. It is evident that the transmit antenna spherical vectors ($\hat{\boldsymbol{\theta}}_t, \hat{\boldsymbol{\phi}}_t$) lie in the same tangential plane (tangent plane 1), where the receive antenna spherical vectors ($\hat{\boldsymbol{\theta}}_r, \hat{\boldsymbol{\phi}}_r$) lie, and both of which are normal to $\hat{\mathbf{k}}_d$, as illustrated in Fig. 12(a), due to the following orthogonality relationship:

$$\hat{\boldsymbol{\phi}}_t \times \hat{\mathbf{k}}_d = \hat{\boldsymbol{\theta}}_t \quad \text{and} \quad \hat{\mathbf{k}}_d \times \hat{\boldsymbol{\theta}}_t = \hat{\boldsymbol{\phi}}_t \quad (\text{B.5a})$$

$$\hat{\mathbf{k}}_d \times \hat{\boldsymbol{\phi}}_r = \hat{\boldsymbol{\theta}}_r \quad \text{and} \quad \hat{\boldsymbol{\theta}}_r \times \hat{\mathbf{k}}_d = \hat{\boldsymbol{\phi}}_r \quad (\text{B.5b})$$

The linear and circular basis vectors (defined in (A.2) and (A.4)] also lie on the same tangent plane since they are rotated versions of spherical vectors defined in their respective coordinate systems. As a result, the transformation matrix, $\underline{\underline{u}}_{t \rightarrow r}$, is, in fact, a rotation matrix between any polarization bases (within the system T or R and between the systems T and R), defined in the same tangential plane. In other words, any polarization states defined along a direct path between the origins of two arbitrary coordinate systems are related via a rotation matrix. One can go from one polarization basis to another one by simply substituting the unit complex polarization vector pairs [i.e., $(\hat{\boldsymbol{\theta}}_t, \hat{\boldsymbol{\phi}}_t)$, $(\hat{\mathbf{u}}_{t1}^R, \hat{\mathbf{u}}_{t2}^L)$, $(\hat{\mathbf{u}}_{t1}^X, \hat{\mathbf{u}}_{t2}^Y)$, $(\hat{\boldsymbol{\theta}}_r, \hat{\boldsymbol{\phi}}_r)$, $(\hat{\mathbf{u}}_{r1}^R, \hat{\mathbf{u}}_{r2}^L)$, and $(\hat{\mathbf{u}}_{r1}^X, \hat{\mathbf{u}}_{r2}^Y)$] in the rotation matrix given in (B.3b).

B. Transmit–Scattering–Receive Configuration

Now, we add an intermediate coordinate system (x', y', z') to represent local scattering processes between transmit and receive antennas, as shown in Fig. 12(b). In this configuration, the transformation involves two rotation matrices; one is from the transmit antenna to the ground system and the other one is from the ground system to the receive antenna. The incoming and outgoing propagation vectors $\hat{\mathbf{k}}_i$ and $\hat{\mathbf{k}}_o$ can be defined and be written in local coordinates by

$$-\hat{\mathbf{k}}_i = \hat{\mathbf{x}}' \sin \theta'_i \cos \phi'_i + \hat{\mathbf{y}}' \sin \theta'_i \sin \phi'_i + \hat{\mathbf{z}}' \cos \theta'_i \quad (\text{B.6a})$$

$$\hat{\mathbf{k}}_o = \hat{\mathbf{x}}' \sin \theta'_o \cos \phi'_o + \hat{\mathbf{y}}' \sin \theta'_o \sin \phi'_o + \hat{\mathbf{z}}' \cos \theta'_o \quad (\text{B.6b})$$

where the angles (θ'_i, ϕ'_i) and (θ'_o, ϕ'_o) represent the angle of incidence and the angle of scattering in the local coordinate system, respectively. The propagation vector, $\hat{\mathbf{k}}_i$, is normal to both the transmit antenna spherical vectors ($\hat{\boldsymbol{\theta}}_t, \hat{\boldsymbol{\phi}}_t$) and the local spherical vectors ($\hat{\boldsymbol{\theta}}'_i, \hat{\boldsymbol{\phi}}'_i$) along the angle (θ'_i, ϕ'_i) while the propagation vector, $\hat{\mathbf{k}}_o$, is normal to both the receive antenna spherical vectors ($\hat{\boldsymbol{\theta}}_r, \hat{\boldsymbol{\phi}}_r$) and the local spherical vectors ($\hat{\boldsymbol{\theta}}'_o, \hat{\boldsymbol{\phi}}'_o$) along the angle (θ'_o, ϕ'_o) . Due to these orthogonality relationships, we can define a tangent plane (tangent plane 2) between the transmit antenna and the ground and can define another tangent plane (tangent plane 3) between the receive antenna and the ground. The unit vectors $(\hat{\mathbf{u}}_{t1}, \hat{\mathbf{u}}_{t2})$ and $(\hat{\mathbf{u}}_{r1}, \hat{\mathbf{u}}_{r2})$ also lie in the tangent planes 2 and 3, respectively. Thus, the rotation matrices from the transmit antenna to the ground and the ground to the receive antenna can be

written as

$$\underline{\underline{u}}_{t \rightarrow g}(\hat{\mathbf{k}}_i) = \begin{bmatrix} \hat{\mathbf{u}}_{t1} \cdot \hat{\mathbf{v}}_i^* & \hat{\mathbf{u}}_{t2} \cdot \hat{\mathbf{v}}_i^* \\ \hat{\mathbf{u}}_{t1} \cdot \hat{\mathbf{h}}_i & \hat{\mathbf{u}}_{t2} \cdot \hat{\mathbf{h}}_i \end{bmatrix} \quad (\text{B.7a})$$

and

$$\underline{\underline{u}}_{g \rightarrow r}(\hat{\mathbf{k}}_o) = \begin{bmatrix} \hat{\mathbf{v}}_o \cdot \hat{\mathbf{u}}_{r1}^* & \hat{\mathbf{h}}_o \cdot \hat{\mathbf{u}}_{r1}^* \\ \hat{\mathbf{v}}_o \cdot \hat{\mathbf{u}}_{r2}^* & \hat{\mathbf{h}}_o \cdot \hat{\mathbf{u}}_{r2}^* \end{bmatrix} \quad (\text{B.7b})$$

where $(\hat{\mathbf{u}}_{t1}, \hat{\mathbf{u}}_{t2})$ and $(\hat{\mathbf{u}}_{r1}, \hat{\mathbf{u}}_{r2})$ can be the linearly polarized or circularly polarized unit vectors as defined in (A.2) and (A.4). The local horizontal polarization vector, $\hat{\mathbf{h}}_o$, for scattered wave is taken parallel to the local ground $(x'y')$ plane. More specifically

$$\hat{\mathbf{h}}_o = \frac{\hat{\mathbf{n}} \times \hat{\mathbf{k}}_o}{|\hat{\mathbf{n}} \times \hat{\mathbf{k}}_o|} = \hat{\boldsymbol{\phi}}'_o \quad (\text{B.8a})$$

The local vertical polarization is taken perpendicular to both $\hat{\mathbf{k}}_o$ and $\hat{\mathbf{h}}_o$; thus,

$$\hat{\mathbf{v}}_o = \hat{\mathbf{h}}_o \times \hat{\mathbf{k}}_o = \hat{\boldsymbol{\theta}}'_o \quad (\text{B.8b})$$

Similarly, the local horizontal polarization vector, $\hat{\mathbf{h}}_i$, for incident wave is taken parallel to the local ground $(x'y')$ plane. More specifically,

$$\hat{\mathbf{h}}_i = \frac{\hat{\mathbf{k}}_i \times \hat{\mathbf{n}}}{|\hat{\mathbf{k}}_i \times \hat{\mathbf{n}}|} = \hat{\boldsymbol{\phi}}'_i \quad (\text{B.9a})$$

The local vertical polarization is taken perpendicular to both $\hat{\mathbf{k}}_i$ and $\hat{\mathbf{h}}_i$; thus,

$$\hat{\mathbf{v}}_i = \hat{\mathbf{k}}_i \times \hat{\mathbf{h}}_i = \hat{\boldsymbol{\theta}}'_i \quad (\text{B.9b})$$

APPENDIX C ANTENNA ROTATION MATRICES

The received field expressions derived in the main text assume knowledge of the relationship between various coordinate systems. In this appendix, we define coordinate transformation between the antenna coordinates and the reference coordinate system. Let us consider the receive antenna here but the same is also applicable to the transmit antenna. The antenna coordinate system is rotated about the z -axis by φ_{0r} in azimuth. Then, the antenna is rotated about the y -axis by $(\pi - \theta_{0r})$ in elevation. The angle φ_{0r} is defined counterclockwise from the x -axis while the angle θ_{0r} is defined counterclockwise from the $-z$ -axis. When $\varphi_{0r} = 0$, the antenna is facing East and when $\varphi_{0r} = \pi/2$, the antenna is facing North. The azimuth rotation is performed for aligning the direction of the incident field from a satellite. When $\theta_{0r} = 0$, the antenna is facing nadir and when $\theta_{0r} = \pi$, the antenna is facing zenith. The angle θ_{0r} represents the observation angle. With these rotations, the antenna y_r -axis will always be parallel to the ground (xy) plane, so that it can represent the horizontal-polarized port when the antenna is linearly polarized. The rotation matrices from the antenna to the reference system in elevation and azimuth planes are,

$$\underline{\underline{G}}^M = \underline{\underline{Q}} \cdot \underline{\underline{G}} \cdot \underline{\underline{Q}}^{-1} = \begin{bmatrix} |g_{RR}|^2 & |g_{RL}|^2 & \text{Re}\{g_{RR}g_{RL}^*\} & -\text{Im}\{g_{RR}g_{RL}^*\} \\ |g_{LR}|^2 & |g_{LL}|^2 & \text{Re}\{g_{LL}g_{LR}^*\} & \text{Im}\{g_{LL}g_{LR}^*\} \\ 2\text{Re}\{g_{RR}g_{LR}^*\} & 2\text{Re}\{g_{LL}g_{RL}^*\} & \text{Re}\{g_{RR}g_{LL}^* - g_{RL}g_{LR}^*\} & -\text{Im}\{g_{RR}g_{LL}^* + g_{RL}g_{LR}^*\} \\ 2\text{Im}\{g_{RR}g_{LR}^*\} & -2\text{Im}\{g_{LL}g_{RL}^*\} & \text{Im}\{g_{RR}g_{LL}^* + g_{RL}g_{LR}^*\} & \text{Re}\{g_{RR}g_{LL}^* + g_{RL}g_{LR}^*\} \end{bmatrix} \quad (\text{D.5})$$

respectively, given by

$$[A]_{\theta_{0r}} = \begin{bmatrix} -\cos\theta_{0r} & 0 & \sin\theta_{0r} \\ 0 & 1 & 0 \\ -\sin\theta_{0r} & 0 & -\cos\theta_{0r} \end{bmatrix} \quad (\text{C.1})$$

$$[A]_{\varphi_{0r}} = \begin{bmatrix} \cos\varphi_{0r} & -\sin\varphi_{0r} & 0 \\ \sin\varphi_{0r} & \cos\varphi_{0r} & 0 \\ 0 & 0 & 1 \end{bmatrix}. \quad (\text{C.1})$$

Because the rotation matrix is orthogonal, transformation in the reverse direction is simply the transpose of the matrix.

APPENDIX D

OUTER PRODUCT MATRICES AND VECTORS

The outer product is defined for two-element vectors by [55]

$$\underline{\underline{P}} = \underline{\underline{b}} \otimes \underline{\underline{b}}^* = \begin{bmatrix} b_1 b_1^* \\ b_1 b_2^* \\ b_2 b_1^* \\ b_2 b_2^* \end{bmatrix} \quad (\text{D.1})$$

and for the two-by-two matrix of a circularly polarized antenna by

$$\underline{\underline{G}} = \underline{\underline{g}} \otimes \underline{\underline{g}}^* = \begin{bmatrix} g_{RR}g_{RR}^* & g_{RL}g_{RL}^* \\ g_{LR}g_{LR}^* & g_{LL}g_{LL}^* \end{bmatrix} \\ = \begin{bmatrix} g_{RR}g_{RR}^* & g_{RR}g_{RL}^* & g_{RL}g_{RR}^* & g_{RL}g_{RL}^* \\ g_{RR}g_{LR}^* & g_{RR}g_{LL}^* & g_{RL}g_{LR}^* & g_{RL}g_{LL}^* \\ g_{LR}g_{RR}^* & g_{LR}g_{RL}^* & g_{LL}g_{RR}^* & g_{LL}g_{RL}^* \\ g_{LR}g_{LR}^* & g_{LR}g_{LL}^* & g_{LL}g_{LR}^* & g_{LL}g_{LL}^* \end{bmatrix}. \quad (\text{D.2})$$

The elements of the coherency vector and matrix are complex, and it is sometimes desirable to describe the wave by real quantities. The modified Stokes vector is commonly used in microwave remote sensing to describe both amplitude and polarization of the wave [43]. It is a transform of the coherency vector. The modified Stokes vector of the total power is given by

$$\underline{\underline{P}}_M = \underline{\underline{Q}} \cdot \underline{\underline{P}} = \begin{bmatrix} |b_1|^2 \\ |b_2|^2 \\ 2\text{Re}\{b_1 b_2^*\} \\ 2\text{Im}\{b_1 b_2^*\} \end{bmatrix} \quad (\text{D.3})$$

where

$$\underline{\underline{Q}} = \begin{bmatrix} 1 & 0 & 0 & 0 \\ 0 & 0 & 0 & 1 \\ 0 & 1 & 1 & 0 \\ 0 & -i & -i & 0 \end{bmatrix} \quad (\text{D.4})$$

Similarly, the four-by-four Mueller matrix of a circularly polarized antenna can be defined for the modified Stokes vector (D.5), as shown at the top of this page.

REFERENCES

- [1] J. Garrison, E. Cardellach, S. Gleason, and S. Katzberg, "Foreword to special issue on reflectometry using global navigation satellite systems and other signals of opportunity (GNSS+R)," *IEEE J. Sel. Topics Appl. Earth Observ. Remote Sens.*, vol. 7, no. 5, pp. 1412–1415, May 2014.
- [2] E. Cardellach, S. Vey, and J. Wickert, "Foreword to the special issue on GNSS reflectometry," *IEEE J. Sel. Topics Appl. Earth Observ. Remote Sens.*, vol. 9, no. 10, pp. 4519–4524, Oct. 2016.
- [3] M. Unwin, P. Jales, J. Tye, C. Gommenginger, G. Foti, and J. Rosello, "Spaceborne GNSS-reflectometry on TechDemoSat-1: Early mission operations and exploitation," *IEEE J. Sel. Topics Appl. Earth Observ. Remote Sens.*, vol. 9, no. 10, pp. 4525–4539, Oct. 2016.
- [4] S. Gleason *et al.*, "Detection and processing of bistatically reflected GPS signals from low Earth orbit for the purpose of ocean remote sensing," *IEEE Trans. Geosci. Remote Sens.*, vol. 43, no. 6, pp. 1229–1241, Jun. 2005.
- [5] C. Ruf *et al.*, "CYGNSS: Enabling the future of hurricane prediction," *IEEE Geosci. Remote Sens. Mag.*, vol. 1, no. 2, pp. 52–67, Jun. 2013.
- [6] V. U. Zavorotny, S. Gleason, E. Cardellach, and A. Camps, "Tutorial on remote sensing using GNSS bistatic radar of opportunity," *IEEE Geosci. Remote Sens. Mag.*, vol. 2, no. 4, pp. 8–45, Dec. 2014.
- [7] N. Rodriguez-Alvarez *et al.*, "Land geophysical parameters retrieval using the interference pattern GNSS-R technique," *IEEE Trans. Geosci. Remote Sens.*, vol. 49, no. 1, pp. 71–84, Jan. 2011.
- [8] A. Alonso-Arroyo *et al.*, "Dual-polarization GNSS-R interference pattern technique for soil moisture mapping," *IEEE J. Sel. Topics Appl. Earth Observ. Remote Sens.*, vol. 7, no. 5, pp. 1533–1544, May 2014.
- [9] A. Egido *et al.*, "Global navigation satellite systems reflectometry as a remote sensing tool for agriculture," *Remote Sens.*, vol. 4, no. 8, pp. 2356–2372, 2012.
- [10] K. M. Larson, J. J. Braun, E. E. Small, V. U. Zavorotny, E. D. Gutmann, and A. L. Bilich, "GPS multipath and its relation to near-surface soil moisture content," *IEEE J. Sel. Topics Appl. Earth Observ. Remote Sens.*, vol. 3, no. 1, pp. 91–99, Mar. 2010.
- [11] C. C. Chew, E. E. Small, K. M. Larson, and V. U. Zavorotny, "Vegetation sensing using GPS-interferometric reflectometry: Theoretical effects of canopy parameters on signal-to-noise ratio data," *IEEE Trans. Geosci. Remote Sens.*, vol. 53, no. 5, pp. 2755–2764, May 2015.
- [12] A. Egido *et al.*, "Airborne GNSS-R polarimetric measurements for soil moisture and above-ground biomass estimation," *IEEE J. Sel. Topics Appl. Earth Observ. Remote Sens.*, vol. 7, no. 5, pp. 1522–1532, May 2014.
- [13] H. Carreno-Luengo, A. Camps, J. Querol, and G. Forte, "First results of a GNSS-R experiment from a stratospheric balloon over boreal forests," *IEEE Trans. Geosci. Remote Sens.*, vol. 54, no. 5, pp. 2652–2663, May 2016.
- [14] C. Chew, R. Shah, C. Zuffada, G. Hajj, D. Masters, and A. J. Mannucci, "Demonstrating soil moisture remote sensing with observations from the UK TechDemoSat-1 satellite mission," *Geophys. Res. Lett.*, vol. 43, no. 7, pp. 3317–3324, 2016.
- [15] A. Camps *et al.*, "Sensitivity of GNSS-R spaceborne observations to soil moisture and vegetation," *IEEE J. Sel. Topics Appl. Earth Observ. Remote Sens.*, vol. 9, no. 10, pp. 4730–4742, Oct. 2016.
- [16] S. V. Nghiem *et al.*, "Wetland monitoring with global navigation satellite system reflectometry," *Earth Space Sci.*, vol. 4, no. 1, pp. 16–39, 2017.
- [17] R. Shah, C. Zuffada, C. Chew, M. Lavalle, X. Xu, and A. Azemati, "Modeling bistatic scattering signatures from sources of opportunity in P-Ka bands," in *Proc. Int. Conf. Electromagn. Adv. Appl. (ICEAA)*, Verona, Italy, Sep. 2017, pp. 1684–1687.
- [18] R. Shah, J. L. Garrison, and M. S. Grant, "Demonstration of bistatic radar for ocean remote sensing using communication satellite signals," *IEEE Geosci. Remote Sens. Lett.*, vol. 9, no. 4, pp. 619–623, Apr. 2012.
- [19] R. Shah, J. L. Garrison, A. Egido, and G. Ruffini, "Bistatic radar measurements of significant wave height using signals of opportunity in L-, S-, and Ku-bands," *IEEE Trans. Geosci. Remote Sens.*, vol. 54, no. 2, pp. 826–841, Feb. 2016.

- [20] A. T. Joseph, M. Deshpande, P. E. O'Neill, and L. Miles, "Development of VHF (240–270 MHz) antennas for SoOp (Signal of Opportunity) receiver for 6U cubesat platforms," in *Proc. 37th Prog. Electromagn. Res. Symp. (PIERS)*, Shanghai, China, 2016, pp. 1–4.
- [21] J. Garrison *et al.*, "Recent results on soil moisture remote sensing using P-band signals of opportunity," in *Proc. Int. Conf. Electromagn. Adv. Appl. (ICEAA)*, Verona, Italy, Sep. 2017, pp. 1604–1607.
- [22] S. Yueh *et al.*, "HydroCube mission concept: P-band signals of opportunity for remote sensing of snow and root zone soil moisture," *Proc. SPIE*, vol. 10423, p. 104230L, Sep. 2017.
- [23] R. Shah *et al.*, "Remote sensing of snow water equivalent using P-band coherent reflection," *IEEE Geosci. Remote Sens. Lett.*, vol. 14, no. 3, pp. 309–313, Mar. 2017.
- [24] M. Kurum, M. Deshpande, A. T. Joseph, P. E. O'Neill, R. Lang, and O. Eroglu, "Development of a coherent bistatic vegetation model for signal of opportunity applications at VHF UHF-bands," in *Proc. IEEE Int. Geosci. Remote Sensing Symp.*, Fort Worth, TX, USA, Jul. 2017, pp. 4894–4896.
- [25] P. Liang, L. E. Pierce, and M. Moghaddam, "Radiative transfer model for microwave bistatic scattering from forest canopies," *IEEE Trans. Geosci. Remote Sens.*, vol. 43, no. 11, pp. 2470–2483, Nov. 2005.
- [26] P. Ferrazzoli, L. Guerriero, N. Pierdicca, and R. Rahmoune, "Forest biomass monitoring with GNSS-R: Theoretical simulations," *Adv. Space Res.*, vol. 47, no. 10, pp. 1823–1832, 2010.
- [27] L. Guerriero, N. Pierdicca, L. Pulvirenti, and P. Ferrazzoli, "Use of satellite radar bistatic measurements for crop monitoring: A simulation study on corn fields," *Remote Sens.*, vol. 5, no. 2, pp. 864–890, 2013.
- [28] N. Pierdicca, L. Guerriero, R. Giusto, M. Brogioni, and A. Egido, "SAVERS: A simulator of GNSS reflections from bare and vegetated soils," *IEEE Trans. Geosci. Remote Sens.*, vol. 52, no. 10, pp. 6542–6554, Oct. 2014.
- [29] X. R. Wu and S. G. Jin, "GNSS-reflectometry: Forest canopies polarization scattering properties and modeling," *Adv. Space Res.*, vol. 54, no. 5, pp. 863–870, 2014.
- [30] L. Thirion-Lefevre, E. Colin-Koeniguer, and C. Dahon, "Bistatic scattering from forest components. Part I: Coherent polarimetric modelling and analysis of simulated results," *Waves Random Complex Media*, vol. 20, no. 1, pp. 36–61, 2010.
- [31] D. E. Kerr, *Propagation of Short Radio Waves*, vol. 13. New York, NY, USA: McGraw-Hill, 1951, sec. 5.4.
- [32] D. M. LeVine, R. Meneghini, R. H. Lang, and S. S. Seker, "Scattering from arbitrarily oriented dielectric disks in the physical optics regime," *J. Opt. Soc. Amer.*, vol. 73, no. 10, pp. 1255–1262, 1983.
- [33] D. M. LeVine, A. Schneider, R. H. Lang, and H. Carter, "Scattering from thin dielectric disks," *IEEE Trans. Antennas Propag.*, vol. AP-33, no. 12, pp. 1410–1413, Dec. 1985.
- [34] S. S. Seker and A. Schneider, "Electromagnetic scattering from a dielectric cylinder of finite length," *IEEE Trans. Antennas Propag.*, vol. AP-36, no. 2, pp. 303–307, Feb. 1988.
- [35] M. A. Karam, A. K. Fung, and Y. M. M. Antar, "Electromagnetic wave scattering from some vegetation samples," *IEEE Trans. Geosci. Remote Sens.*, vol. GRS-26, no. 6, pp. 799–808, Nov. 1988.
- [36] W. Wasylkiwskyj, "Response of an antenna to arbitrary incident fields," in *Proc. Int. Symp. Antennas Propag. Soc.*, Washington, DC, USA, Jul. 2005, pp. 39–42.
- [37] H. Mott, *Polarization in Antennas and Radar*. New York, NY, USA: Wiley, 1986.
- [38] R. H. Lang, R. Landry, O. Kavaklioglu, and J.-C. Deguise, "Simulation of microwave backscatter from a red pine stand," *Proc. SPIE*, vol. 2314, pp. 538–549, Jan. 1994.
- [39] R. H. Lang, "Electromagnetic backscattering from a sparse distribution of lossy dielectric scatterers," *Radio Sci.*, vol. 16, no. 1, pp. 15–30, 1981.
- [40] L. L. Foldy, "The multiple scattering of waves. I. General theory of isotropic scattering by randomly distributed scatterers," *Phys. Rev.*, vol. 67, pp. 107–119, Feb. 1945.
- [41] M. Lax, "Multiple scattering of waves," *Rev. Mod. Phys.*, vol. 23, pp. 287–310, Oct. 1951.
- [42] B. J. Choudhury, T. J. Schmutge, A. Chang, and R. W. Newton, "Effect of surface roughness on the microwave emission from soils," *J. Geophys. Res., Oceans*, vol. 84, no. C9, pp. 5699–5706, 1979.
- [43] L. Tsang, J. A. Kong, and R. T. Shin, *Theory of Microwave Remote Sensing*. New York, NY, USA: Wiley, 1985.
- [44] M. Kurum, "L-band estimation of forest canopy attenuation by a time-domain analysis of radar backscatter response," Ph.D. dissertation, Dept. Elect. Comput. Eng., George Washington Univ., Washington, DC, USA, 2009.
- [45] A. Ishimaru, *Wave Propagation and Scattering in Random Media*, vol. 1. New York, NY, USA: Academic, 1978, ch. 5.4.
- [46] S. J. Katzberg and J. L. Garrison, "Utilizing GPS to determine ionospheric delay over the ocean," NASA, Washington, DC, USA, Tech. Rep. NASA-TM-4750, 1996.
- [47] G. A. Hajj and C. Zuffada, "Theoretical description of a bistatic system for ocean altimetry using the GPS signal," *Radio Sci.*, vol. 38, no. 5, pp. 10-1–10-19, 2003.
- [48] M. Kurum, R. H. Lang, P. E. O'Neill, A. T. Joseph, T. J. Jackson, and M. H. Cosh, "A first-order radiative transfer model for microwave radiometry of forest canopies at L-band," *IEEE Trans. Geosci. Remote Sens.*, vol. 49, no. 9, pp. 3167–3179, Sep. 2011.
- [49] T. Castel, A. Beaudoin, N. Floury, T. L. Toan, Y. Caraglio, and J. F. Barzci, "Deriving forest canopy parameters for backscatter models using the AMAP architectural plant model," *IEEE Trans. Geosci. Remote Sens.*, vol. 39, no. 3, pp. 571–583, Mar. 2001.
- [50] Y.-C. Lin and K. Sarabandi, "A Monte Carlo coherent scattering model for forest canopies using fractal-generated trees," *IEEE Trans. Geosci. Remote Sens.*, vol. 37, no. 1, pp. 440–451, Jan. 1999.
- [51] S. J. Katzberg, O. Torres, M. S. Grant, and D. Masters, "Utilizing calibrated GPS reflected signals to estimate soil reflectivity and dielectric constant: Results from SMEX02," *Remote Sens. Environ.*, vol. 100, no. 1, pp. 17–28, Jan. 2006.
- [52] R. H. Lang and P. de Mattheis, "Microwave scattering models for cylindrical vegetation components," *Prog. Electromagn. Res.*, vol. 55, pp. 307–333, 2005.
- [53] A. Ludwig, "The definition of cross polarization," *IEEE Trans. Antennas Propag.*, vol. AP-21, no. 1, pp. 116–119, Jan. 1973.
- [54] W.-M. Boemer, W.-L. Yan, A.-Q. Xi, and Y. Yamaguchi, "Basic concepts of radar polarimetry," in *Direct and Inverse Methods in Radar Polarimetry*. Dordrecht, The Netherlands: Kluwer, 1992, pp. 155–245.
- [55] J. P. Hamaker, J. D. Bregman, and R. J. Sault, "Understanding radio polarimetry. I. Mathematical foundations," *Astron. Astrophys., Suppl. Ser.*, vol. 117, no. 1, pp. 137–147, 1996.



Mehmet Kurum (M'08–SM'14) received the B.S. degree in electrical and electronics engineering from Bogaziçi University, Istanbul, Turkey, in 2003, and the M.S. and Ph.D. degrees in electrical engineering from George Washington University, Washington, DC, USA, in 2005 and 2009, respectively.

He held a post-doctoral position at the Hydrological Sciences Laboratory, NASA Goddard Space Flight Center, Greenbelt, MD, USA. In 2016, he joined the Department of Electrical and Computer Engineering, Mississippi State University, Mississippi State, MS, USA, as an Assistant Professor. His research interests include microwave and millimeter-wave remote sensing, RF sensors and systems, radiation and scattering theory, and signals of opportunity.

Dr. Kurum was a recipient of the Leopold B. Felsen Award for excellence in electromagnetic in 2013 and the International Union of Radio Science (URSI) Young Scientist Award in 2014. He serves as an Early Career Representative for the International URSI Commission F (Wave Propagation and Remote Sensing).



Manohar Deshpande (M'02–SM'04) received the B.E., M.Tech., and Ph.D. degrees from IIT Kharagpur, Kharagpur, India, in 1970, 1972, and 1980, respectively.

He was an Associate Professor with IIT Kharagpur, where he guided several Ph.D. and M.Tech. students, from 1982 to 1989. He was an Antenna Design Engineer with the NASA Langley Research Center, Hampton, VA, USA, from 1990 to 2005, where he has developed antenna analysis and design tools based on the method of moment, finite-element method, and hybrid methods. Since 2005, he has been a Senior RF Engineer with the Microwave Instrument Technology Branch (Code 555), NASA Goddard Space Flight Center, Greenbelt, MD, USA. Most of his work has been published in the IEEE TRANSACTIONS ON ANTENNAS AND PROPAGATION and the IEEE MICROWAVE THEORY AND TECHNIQUES.



Alicia T. Joseph received the B.S. degree in environmental science from Medgar Evers College, City University of New York, Brooklyn, NY, USA, in 1997, the M.S. degree in environmental and occupational health science from Hunter College, New York, NY, USA, in 2000, the M.S. degree in geography and environmental engineering from Johns Hopkins University, Baltimore, MD, USA, in 2004, and the Ph.D. degree in the analysis of the microwave optical depth using physical and semiempirical emission models from the University of Maryland, College Park, MD, USA, in 2010.

She is currently a Research Physical Scientist with the Hydrological Sciences Laboratory, NASA Goddard Space Flight Center, Greenbelt, MD, USA. Her research interests include the microwave remote sensing of soil moisture retrieval.

Dr. Joseph was a recipient of the National Association for Equal Opportunity in Higher Education Distinguished Alumni Award in 2007, the 7th Annual Medgar Evers College Legacy Award in 2007, and the NASA Earth Sciences HOBII Award for outstanding scientific achievement in 2012.



Peggy E. O'Neill (F'16) received the B.S. degree (*summa cum laude*) in geography from Northern Illinois University, DeKalb, IL, USA, in 1976, and the M.A. degree in geography from the University of California at Santa Barbara, Santa Barbara, CA, USA, in 1979.

She has done postgraduate research in civil and environmental engineering at Cornell University, Ithaca, NY, USA. Since 1980, she has been a Physical Scientist with the Hydrological Sciences Laboratory, NASA Goddard Space Flight Center, Greenbelt, MD, USA, where she conducts research in soil moisture retrieval and land surface hydrology, primarily through microwave remote sensing techniques, and is currently the SMAP Deputy Project Scientist.



Roger H. Lang (F'89–LF'06) received the B.S. and M.S. degrees in electrical engineering and the Ph.D. degree in electrophysics from the Polytechnic Institute of Brooklyn, New York, NY, USA, in 1962, 1964, and 1968, respectively.

He did post-doctoral work in random media under J. Keller at the Courant Institute of Mathematical Sciences, New York University, New York, NY, USA. He is currently the L. Stanley Crane Professor of engineering and applied science with George Washington University, Washington, DC, USA. He has been a member of the NASA Aquarius Science Team, where he is involved in the remote sensing of seawater salinity. He is known for the early development of the discrete scattering model for vegetation. His research interests include microwave remote sensing and electromagnetic wave propagation.

Dr. Lang is a member of the Editorial Board of *Waves in Random and Complex Media* and has been the Chair of the International URSI Commission F. He is an active participant with the IEEE Geoscience and Remote Sensing Society. He has been an Associate Editor of *Microwave Scattering and Propagation*, and a Co-Chairman of the Technical Program Committee for the IGARSS'90 meeting held at College Park, MD, USA, in 1990.



Orhan Eroglu (M'17) received the B.S. degree in computer engineering from Bogaziçi University, Istanbul, Turkey, in 2009, and the M.S. degree in computer engineering from Turkish Air Force Academy, Aeronautics and Space Technology Institute, Istanbul, in 2013. He is currently pursuing the Ph.D. degree with the Electrical and Computer Engineering Department, Mississippi State University, Mississippi State, MS, USA.

He was a Researcher and a Senior Researcher with the Scientific and Technological Research Council of Turkey (TUBITAK), Informatics and Information Security Research Center (BILGEM), Gebze, Turkey, from 2009 to 2016. He is a NASA Earth and Space Science Fellow with his study entitled "Unveiling CYGNSS Land Signatures for High Spatiotemporal Soil Moisture Estimation." His research interests include data analytics and machine learning in remote sensing applications and signal of opportunity.